Review

Perovskite-Based X-ray Detectors

Chen-Fu Lin 1,*, Kuo-Wei Huang 1,2, Yen-Ting Chen 1, Sung-Lin Hsueh 1 [ID], Ming-Hsien Li 3,* [ID] and Peter Chen 1,4,5,6,*

1   Department of Photonics, National Cheng Kung University, Tainan 70101, Taiwan
2   Photovoltaic Technology Division, Green Energy & Environment Research Laboratories, Industrial Technology Research Institute, Tainan 71150, Taiwan
3   Department of Applied Materials and Optoelectronic Engineering, National Chi Nan University, Nantou 54561, Taiwan
4   Core Facility Center (CFC), National Cheng Kung University, Tainan 70101, Taiwan
5   Hierarchical Green-Energy Materials (Hi-GEM) Research Center, National Cheng Kung University, Tainan 70101, Taiwan
6   Program on Key Materials, Academy of Innovative Semiconductor and Sustainable Manufacturing, National Cheng Kung University, Tainan 70101, Taiwan
*   Correspondence: sunboy@mail.mse.ncku.edu.tw (C.-F.L.); mhli1125@ncnu.edu.tw (M.-H.L.); petercyc@ncku.edu.tw (P.C.)

Abstract: X-ray detection has widespread applications in medical diagnosis, non-destructive industrial radiography and safety inspection, and especially, medical diagnosis realized by medical X-ray detectors is presenting an increasing demand. Perovskite materials are excellent candidates for high-energy radiation detection based on their promising material properties such as excellent carrier transport capability and high effective atomic number. In this review paper, we introduce X-ray detectors using all kinds of halide perovskite materials along with various crystal structures and discuss their device performance in detail. Single-crystal perovskite was first fabricated as an active material for X-ray detectors, having excellent performance under X-ray illumination due to its superior photoelectric properties of X-ray attenuation with μm thickness. The X-ray detector based on inorganic perovskite shows good environmental stability and high X-ray sensitivity. Owing to anisotropic carrier transport capability, two-dimensional layered perovskites with a preferred orientation parallel to the substrate can effectively suppress the dark current of the device despite poor light response to X-rays, resulting in lower sensitivity for the device. Double perovskite applied for X-ray detectors shows better attenuation of X-rays due to the introduction of high-atomic-numbered elements. Additionally, its stable crystal structure can effectively lower the dark current of X-ray detectors. Environmentally friendly lead-free perovskite exhibits potential application in X-ray detectors by virtue of its high attenuation of X-rays. In the last section, we specifically introduce the up-scaling process technology for fabricating large-area and thick perovskite films for X-ray detectors, which is critical for the commercialization and mass production of perovskite-based X-ray detectors.

Keywords: X-ray detector; photoelectronic effect; perovskite; inorganic perovskite; two-dimensional layered perovskite; double perovskite; lead-free perovskite

1. Introduction

X-rays are a form of high-energy radiation that is extremely penetrating and unobservable to the naked eye. When X-rays pass through an object, it will be affected by the object and its radiation intensity will be attenuated to ionize the electron from the object. As a result of exposure to different doses and energies of X-rays, the absorber layer produces different output signals, which are then converted into observable digital images by the thin-film transistor arrays (TFT arrays) underneath the absorber layer [1]. With the development of ionizing radiation technology, X-ray detection has a wider application in medical diagnosis, non-destructive industrial radiography and safety inspection,

and especially, medical diagnosis realized by medical X-ray detectors is presenting an increasing demand. Due to the low X-ray response of traditional medical X-ray detectors, high-dose X-ray exposure and prolonged exposure time are required, which have negative effects on the subject's body. Therefore, it is necessary to develop low-cost, low-risk and high-quality X-ray detectors with high sensitivity and a low detection limit. In recent years, many researchers have proposed to replace the commonly used X-ray absorber layer of amorphous selenium (a-Se) with halide perovskite materials because of their high atomic number, long carrier lifetime, high defect tolerance, long electron–hole drift length, large bandgap and high X-ray absorption coefficient. A high X-ray absorption coefficient and other photoelectric characteristics make halide perovskite materials excellent candidates for X-ray detection.

1.1. Indirect-Conversion X-ray Detectors

The basic component of an indirect X-ray detector is a scintillator that converts high-energy photons, such as X-rays and gamma rays, into low-energy ultraviolet or visible light. These low-energy photons detected by an array of photoelectric diodes behind the scintillator are further converted into recognizable signals. Traditionally used materials in scintillators for indirect X-ray detection, such as CsI, NaI, $Bi_4Ge_3O_{12}$, $CdWO_4$ and $(Lu,Y)_2SiO_5$ [2–6], are well developed with some drawbacks, including complex and expensive processes, radioactive afterglow and untunable scintillation caused by uncontrollable transition energy gaps. These drawbacks could be addressed by applying the emerging perovskite as a scintillator material because of its tunable energy gap and short photoluminescence (PL) lifetime [7,8]. Since 1993, researchers have observed strong PL emission of $CsPbCl_3$ with an emission lifetime in the nanosecond timescale, and it was considered a potential material for scintillators [9]. By 1995, Belsky's team published the first research paper using perovskite as a scintillator [10]. In 2002, two-dimensional layered perovskite exhibited a strong radiative emission at room temperature [11]. To date, many research teams have developed efficient perovskite scintillators.

1.2. Direct-Conversion X-ray Detectors

A direct X-ray detector mainly consists of an absorber layer and a TFT array, in which the absorber layer is directly exposed to the X-ray and ionized to form different intensities of electronic signals. The electronic signals read out by the TFT array eventually show the digital image. Currently, the commercial product of a direct X-ray plate mainly employs stable a-Se due to its facile deposition directly onto large-area TFT array substrates by a low-temperature process [12]. However, due to the low atomic number of selenium, it has poor X-ray blocking and absorption ability, and the charge transport capability of selenium is also poor. It requires a large applied electrical field to drive charge carriers to the electrode to improve the carrier collection efficiency. Many research teams have successively searched for alternative materials with high X-ray absorption ability, such as mercury iodide (HgI_2), lead iodide (PbI_2), lead oxide (PbO) and cadmium telluride (CdTe) [13–16]. These materials have shown their potential for large-area hard X-ray (>30 keV) imaging, but these materials still have many difficulties to overcome in terms of film growth, device fabrication and operation. In recent years, emerging perovskite is a potential candidate for direct X-ray detectors due to the advantages of a low-cost solution process, excellent X-ray attenuation and absorption capabilities, high carrier mobility and long carrier lifetime. Typically, perovskite-based X-ray detectors apply two main device architectures: photoconductor- and photodiode-type structures. In the photoconductor-type structure, the intrinsic perovskite semiconductor serving as an X-ray active layer is sandwiched between two ohmic metal electrodes. When the X-ray is irradiated onto the photoconductor-type device, carriers generated by the X-ray are separated and driven by the bias voltage and then collected by the two metal electrodes. For the photodiode-type structure, which is similar to the photovoltaic devices, the perovskite active layer is in contact with at least one selective contact (n- or p-type semiconductor) to produce Schottky,

p–n or p–i–n heterojunctions. The junction barrier in this device structure can facilitate the carrier's separation under a lower bias voltage and reduce the dark current. In the past few years, various perovskite materials have been applied for direct X-ray detectors to deliver remarkable device performance with high detective sensitivity and a low detection limit [17,18].

1.3. Perovskite-Based X-ray Detectors

Halide perovskite, with a general formula of ABX_3 (A-site cation: $CH_3NH_3^+$ (methylammonium, MA^+), $HC(NH_2)_2^+$ (formamidinium, FA^+) and Cs^+; B-site cation: Sn^{2+} and Pb^{2+}; X-site anion: Cl^-, Br^- and I^-), has become a promising semiconductor material for optoelectronic applications. Halide perovskite was initially employed as a light absorber in photovoltaic devices, and its photovoltaic performance quickly reached a high power conversion efficiency that is comparable to that of conventional Si- and CdTe-based solar cells [19]. The great achievement of perovskite in solar cells arouses their application in various optoelectronic devices [20]. Based on promising material properties such as excellent carrier transport properties, high effective atomic number and tunable composition of perovskite, perovskite materials are excellent candidates for high-energy radiation detection. First, in 2013, Kanatzidis' team successfully demonstrated melt-growth $CsPbBr_3$ for direct X-ray radiation detection, initiating the development of perovskite-based X-ray detectors [21]. Soon after, in 2017, Park's team fabricated a polycrystalline $MAPbI_3$ perovskite as an X-ray absorber layer that is deposited on a large-area TFT substrate using a doctor blade-coating method. The sensitivity of the fabricated device reached 1.1×10^4 $\mu C \cdot Gy_{air}^{-1} \cdot cm^{-2}$, which is much larger than that of common commercial X-ray detectors using a-Se [22]. In 2019, Pan's team used the hot-pressing method to fabricate a quasi-monocrystalline structure of $CsPbBr_3$, and the sensitivity of the device reached 5.5×10^4 $\mu C \cdot Gy_{air}^{-1} \cdot cm^{-2}$, which is still the highest sensitivity for X-ray detectors employing polycrystalline inorganic perovskites [23]. Glushkova's team used 3D jet-printing in 2021 to fabricate a single-crystal $MAPbI_3$-based X-ray detector with a record sensitivity. The sensitivity of this detector is up to 2.2×10^8 $\mu C \cdot Gy_{air}^{-1} \cdot cm^{-2}$, which is several orders of magnitude higher than that of the a-Se counterpart (20 $\mu C \cdot Gy_{air}^{-1} \cdot cm^{-2}$) [24]. These developments demonstrate the advantages of perovskite over amorphous selenium applied in high-energy radiation detection.

2. Principles of High-Energy Radiation Detectors

2.1. Fundamentals of X-ray Detection Material

2.1.1. X-ray Attenuation Ratio (ε)

When X-rays pass through matter, some interactions will occur with that matter, such as photoelectric effects, Rayleigh scattering, Compton scattering, etc. At the same time, the incident X-rays will be attenuated due to these interactions. The attenuation of X-rays can be calculated according to the Beer–Lambert law:

$$I = I_0 e^{[-(\frac{\mu}{\rho})x]} \tag{1}$$

where I is the intensity of X-rays attenuated by the matter, I_0 is the original intensity of incident X-ray, μ is the linear attenuation coefficient, ρ is the density of matter and x is the distance of X-ray penetration. Scientists often use the linear attenuation coefficient (μ) to compare the attenuation ability of various materials under X-ray exposure. The linear attenuation coefficient is a constant used to describe the attenuation of incident photons per unit thickness of the material, and it takes into account all possible interactions between the matter and the photon. The linear attenuation coefficient in cm^{-1} is proportional to $\frac{Z^4}{E_{ph}^3}$, where Z is the atomic number of the material and E_{ph} is the energy of the incident photon. Sometimes the mass attenuation coefficient in $cm^2 g^{-1}$ is also used to define the attenuation capability, which is defined as the linear attenuation coefficient per unit density

of the material, yielding a value that is constant for a given element or compound. The attenuation ratio (ε) of a material with a thickness of L can be expressed as follows:

$$\varepsilon = 1 - e^{(-\mu L)} \tag{2}$$

Based on the previous equations, the photon absorption rate (φ), which represents the number of X-ray photons absorbed per second, can be expressed in Equation (3) [23]:

$$\varphi = \frac{\varepsilon D m}{E_{ph}} \tag{3}$$

where D is the dose rate and m is the material mass.

2.1.2. Ionization Energy (W)

The ionization energy (W) represents the energy required to generate a free electron–hole pair for the target material. For most semiconductor materials, the ionization energy is only related to its energy gap (Eg) and follows the empirical formula [25]:

$$W = A * Eg + B \tag{4}$$

where A and B are constants. The literature indicates that the ionization energy of most perovskite materials is W = 2Eg + 1.43 eV, which is nearly an order of magnitude lower than that of amorphous selenium [23]. Under the same dose of high-energy photons, the number of free electron–hole pairs generated in perovskites is an order of magnitude higher than that of amorphous selenium. The result suggests that perovskite is an excellent candidate material as the absorber layer for a high-energy photon detector.

2.1.3. Charge Collection Efficiency (CCE)

The high-energy photon incident on a material will transfer its energy to the inner shell electron of the material and excite an electron, and the kinetic energy of this photoelectron is equal to the energy of a high-energy photon minus the ionization energy of the material. This photoelectron further ionizes other low-ionization-energy electrons in the material. Theoretically, the number of electron–hole pairs produced by a high-energy photon can be calculated by the formula:

$$\beta = \frac{E_{ph}}{W} \tag{5}$$

where β is the maximum number of photo-generated carriers. When the device is driven by an external electric field under illumination, the light-generated electron–hole pairs will drift to the electrode and be extracted to generate an electronic signal. The theoretically maximum photo-generated current (I_P) can be calculated by the equation:

$$I_p = \varphi \beta e \tag{6}$$

where e is the quantity of electron charge. The actual number of carriers that can be finally collected by the electrodes is reduced due to carrier recombination, carrier trapping, etc. Considering the carrier loss, the modified Hecht equation [26] can be used to present the actual photogeneration current collected by the electrodes:

$$I = I_0 \frac{\mu \tau V}{L^2} \frac{1 - \exp\left(-\frac{L^2}{\mu \tau V}\right)}{1 + \frac{L}{V} \frac{s}{\mu}} \tag{7}$$

where I_0 is the saturation photocurrent, L is the material layer thickness, V is the applied bias voltage, s is the surface recombination rate, τ is the carrier lifetime and μ is the carrier mobility, and the charge collection efficiency (CCE) is defined as [27]:

$$CCE = \frac{\mu\tau V}{L^2}\left[1 - e^{\left(-\frac{L^2}{\mu\tau V}\right)}\right] \tag{8}$$

2.2. Parameters of X-ray Detectors

2.2.1. Dark Current (I_{dark})

Dark current is the current generated by the device due to its environment in the absence of X-ray irradiation. The dark current in the detector belongs to the background noise signal. Excessive dark currents result in indistinguishable electronic signals, reduce the sensitivity and increase the minimum detection limit of the device when the device is exposed to X-ray irradiation.

2.2.2. Sensitivity (S)

Sensitivity is a criterion to describe the ability of a direct X-ray detector to convert an incident X-ray photon into an electronic signal. Briefly, an X-ray detector with high sensitivity can produce a large electronic signal under the same exposure dose rate and enhance electronic signal identification. The sensitivity (S) of a direct X-ray detector is defined as the current density difference between the output current density with and without X-ray irradiation over the X-ray irradiation dose rate of D [28].

$$S = \frac{I_{\text{X-ray}} - I_{dark}}{DA} \tag{9}$$

where I_{dark} is the dark current, $I_{\text{X-ray}}$ is the output current ($I_{signal} + I_{dark}$) with X-ray irradiation, D is the exposure dose rate (unit in $Gy{\cdot}s^{-1}$ or $R{\cdot}s^{-1}$) and A is the sensing area. Some researchers also define the device sensitivity as [29]

$$S = \frac{I_{\text{X-ray}} - I_{dark}}{DV} \tag{10}$$

where V is the sensor sensing volume. The device sensitivity is affected by the X-ray attenuation, electron–hole generation, carrier extraction and photoconductivity gain.

2.2.3. Limit of Detection

According to the definition of the International Union of Pure and Applied Chemistry (IUPAC) [30], the lowest detection limit is the value at which the X-ray detector can still produce a signal-to-noise ratio (SNR) = 3 at a specific exposure dose, and the corresponding exposure dose is defined as the lowest dose rate. The signal-to-noise is shown in the following formula:

$$SNR = \frac{J_s}{J_n} \tag{11}$$

where J_s is the difference between the average photocurrent density (J_p) and the dark current density (J_d) and J_n is the noise current density, defined as the standard deviation of photocurrent density, which can be expressed as

$$J_n = \sqrt{\frac{1}{N}\sum_{i}^{N}\left(J_i - J_p\right)^2} \tag{12}$$

The lower the detection limit of the X-ray detector achieved, the lower the exposure required for the device.

2.2.4. Mobility-Lifetime Product (μτ)

Mobility-lifetime product is an important parameter that is used to describe the quality of an X-ray photoactive layer. A high mobility-lifetime product enhances the carrier collection efficiency of the detector and improves the device's performance. Theoretically, the mobility-lifetime product value is correlated with the CCE by the Hecht equation, as presented in Equation (8) [26].

2.2.5. Response Time

Response time is used to quantify the sensing speed of a detector. The general definition of response time is usually expressed in the form of rising time and falling time. Rising time is the time of photocurrent required to rise from 10% to 90% of the saturated photocurrent when the X-ray detector is exposed to X-ray irradiation, while the falling time is the time of photocurrent required to fall from 90% to 10% of the saturated photocurrent when the X-ray irradiation is off. The falling time is usually longer than the rising time because of the trap or defect states in the material. The ideal X-ray detectors should have a short response time, which not only reduces the exposure time to X-rays but also facilitates their use in X-ray imaging, such as fluoroscopy. The response time of perovskite-based X-ray detectors varies from a few milliseconds to sub-milliseconds, which makes it difficult to apply them in X-ray image acquisition at high frame rates.

3. Classification of Perovskite-Based X-ray Detectors

Single crystals (SCs), wafers and film types of halide perovskites are developed for X-ray detection. The perovskite single crystals and wafers have few grain boundaries and a high μτ value. Film-type perovskite could be directly deposited onto a flexible substrate with a large-size area for specific X-ray detection. Therefore, we highlight some advanced works in halide perovskite-based X-ray detectors using perovskite SCs, wafers and films.

3.1. Three-Dimensional (3D) ABX_3 Structure

3.1.1. Organic/Inorganic 3D ABX_3 Structure

Single Crystals (SCs)

An X-ray detector using single-crystal perovskite usually has high X-ray sensitivity, high bulk resistivity and a low trap density due to its good material quality with smooth morphology. The inverse temperature crystallization (ITC) method is a traditional method for fabricating single crystals. The ITC process can shorten the reaction time and prepare high-quality perovskite single crystals. Many studies have demonstrated the fabrication of organic–inorganic hybrid perovskite single crystals, such as $MAPbI_3$ and $MAPbBr_3$. Among them, Song et al. [31] used the surface passivation strategy with methylammonium iodide (MAI) to remarkably increase the ion migration activation energy of $MAPbI_3$ SCs (as seen in Figure 1a) and effectively stabilize the dark current of a coplanar-structure device. Under a large electric field of 100 V mm^{-1}, the as-fabricated device achieved a record-high sensitivity above 700,000 μC·Gy$_{air}$$^{-1}$·cm^{-2} (X-ray irradiation with energy up to 50 keV). Wang et al. [32] used the continuous mass transport process (CMTP) with steady self-supply to improve the carrier mobility of single-crystal $MAPbI_3$ perovskite. The single-crystal $MAPbI_3$ perovskite prepared by CMTP exhibited a low trap density of 4.5×10^9 cm^{-3}, a high carrier mobility of 150.2 cm^2·V^{-1}·s^{-1} and a high mobility–lifetime product of 1.6×10^{-3} cm^2·V^{-1}. Under soft X-ray irradiation with a Cu Kα peak energy at 8 kV, the X-ray detector using $MAPbI_3$ single crystal prepared by CMTP delivered a superior X-ray response than that prepared by ITC. Huang et al. [33] employed A-site cation engineering to fabricate alloyed $DMAMAPbI_3$ (DMA: dimethylammonium) and $GAMAPbI_3$ (GA: guanidinium) SCs via ITC. Alloying large-sized A-site cations of DMA$^+$ or GA$^+$ can improve the charge collection efficiency presumably due to the increased defect formation energy and the decreased electron–phonon coupling strength. The X-ray detectors based on $GAMAPbI_3$ exhibited the best performance with a sensitivity of 2.31×10^4 μC·Gy^{-1}·cm^{-2} and a detection limit of 16.9 nGy$_{air}$·s^{-1}. Ye et al. [34] used seed

dissolution–regrowth to improve the crystal quality of cuboid $MAPbI_3$. The $MAPbI_3$-based X-ray detector delivered a sensitivity of 968.9 $\mu C \cdot Gy^{-1} \cdot cm^{-2}$ under −1 V bias. Later, Geng et al. [35] controlled the temperature gradient (TG) during the synthesis of $MAPbI_3$ SCs to effectively reduce the trap density and improve the crystal quality (refer to Figure 1b). Such an improvement led to the as-fabricated X-ray detector having a boosted sensitivity of 1471.7 $\mu C \cdot Gy_{air}^{-1} \cdot cm^{-2}$ under a low electric field of 3.3 $V \cdot mm^{-1}$. Shrestha et al. [36] reported a mechanical sintering process to fabricate wafer-sized perovskite with polycrystalline $MAPbI_3$ that was several hundred micrometers thick. The fabricated device showed a sensitivity of 2527 $\mu C \cdot Gy_{air}^{-1} \cdot cm^{-2}$ under 70 kV_p X-ray irradiation and a high ambipolar mobility–lifetime product of 2×10^{-4} $cm^2 \cdot V^{-1}$.

The $MAPbBr_3$ perovskite exhibits a higher stability than the $MAPbI_3$ one and a wider absorption range for visible light than the $MAPbCl_3$ one. Geng et al. [37] synthesized a high-quality $MAPbBr_3$ SC with a high mobility–lifetime product of 4.1×10^{-2} $cm^2 \cdot V^{-1}$ by the ITC process, and its application for the X-ray detector exhibited a high sensitivity up to 259.9 $\mu C \cdot Gy_{air}^{-1} \cdot cm^{-2}$ under the X-ray irradiation of 39 keV. Xu et al. [38] fabricated a reliable and sensitive $MAPbBr_3$-based X-ray detector with a high on–off photocurrent ratio and a fast response based on the Au-$MAPbBr_3$–Al sandwich structure (as seen in Figure 1c). The Schottky barrier built at the $MAPbBr_3$–Al heterojunction effectively suppressed the leakage current and enhanced the charge collection capability. Eventually, the corresponding device exhibited a high sensitivity of 359 $\mu C \cdot Gy_{air}^{-1} \cdot cm^{-2}$ and a fast response time of 76.2 ± 2.5 μs at room temperature. To improve the sensitivity of the X-ray detector, Pan et al. [39] proposed a perovskite–perovskite heterojunction formed by the epitaxial growth of $MAPbBr_3$ SCs on Bi^{3+}-doped $MAPbCl_3$ SCs. The perovskite–perovskite heterojunction shows a relatively low trap density and enhanced built-in potential. The resultant X-ray detector delivered a fast response time of 4.89 μs and a high sensitivity of 1.72×10^3 $\mu C \cdot Gy_{air}^{-1} \cdot cm^{-2}$ for 50 kVp X-ray photon illumination under a reverse electric field of 31.5 $V \cdot mm^{-1}$. Fan et al. [40] showed an effective method to fabricate mixed-cation $MA_xCs_{1-x}PbBr_3$ SCs with the assistance of antisolvent and successfully used the mixed-cation perovskite SCs to produce a highly sensitive X-ray detector with a symmetrical sandwich structure. Their bandgap can be tuned from 2.25 to 2.16 eV by increasing the MA composition, and adding MA at the A site results in significantly improved electronic properties of the mixed-cation perovskite involving lower trap density, higher mobility and higher conductivity. The X-ray detector employing mixed-cation $MA_xCs_{1-x}PbBr_3$ perovskite achieved a remarkable sensitivity of up to 2017 $\mu C \cdot Gy_{air}^{-1} \cdot cm^{-2}$ and a detection limit of 1.2×10^3 $nGy_{air} \cdot s^{-1}$ under an applied voltage of 1 V.

Although thermal evaporation is an expensive process for fabricating perovskite SC, it is feasible to produce higher-quality SCs with a larger size than those prepared by the solution process. Liu et al. [41] fabricated stable, inch-sized and multi-component perovskite (FAMACs) SCs, in which the MA^+ and cesium (Cs^+) cations and the bromine (Br^-) anion were mixed into the $FAPbI_3$ lattice by thermal evaporation (refer to Figure 1d). Their application for the X-ray detector showed a high sensitivity of $(3.5 \pm 0.2) \times 10^6$ $\mu C \cdot Gy_{air}^{-1} \cdot cm^{-2}$ and a detection limit of 42 $nGy_{air} \cdot s^{-1}$ under 40 keV X-ray radiation. This work demonstrated the exclusive ability to recognize the images of steel objects in a closed opaque black plastic box by X-ray detection.
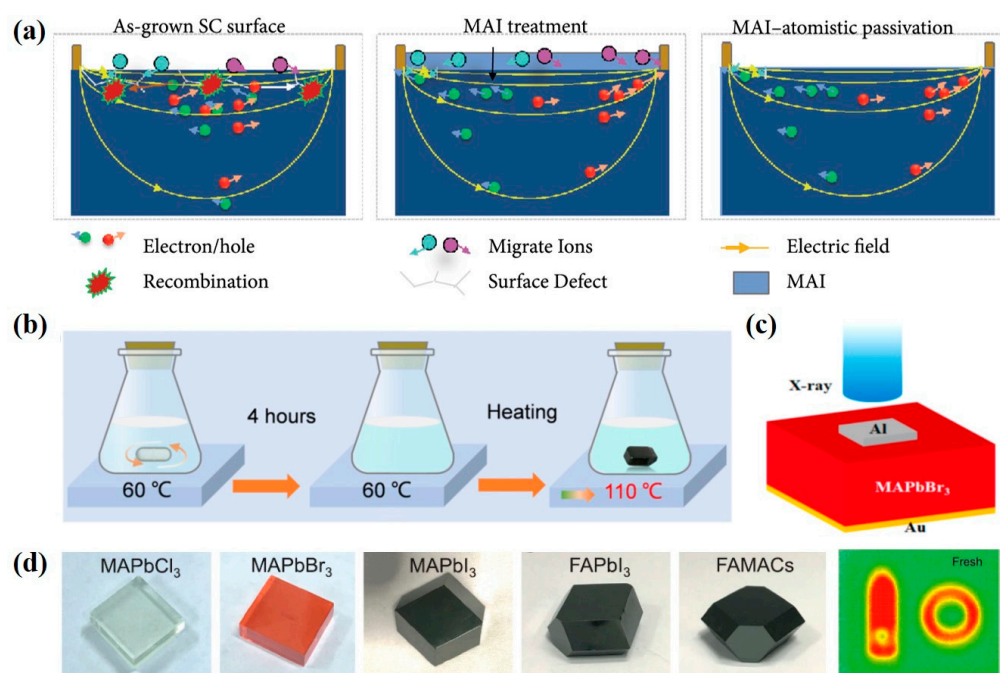
Figure 1. Application of organic–inorganic hybrid perovskite SCs in X-ray detectors. (**a**) Schematic diagram of the working principle for the X-ray detector with different surface treatments [31]. (**b**) Schematic diagram of the crystallization process for the MAPbI$_3$ SCs with small and large temperature gradients [35]. (**c**) Schematic diagram of a device with Au/MAPbBr$_3$ SCs/Al architecture [38]. (**d**) Different perovskite SCs fabricated by thermal evaporation and X-ray images of a closed black plastic box measured by the FAMACs-SC-based X-ray detector [41].

Thin Films

There are only a few studies about the fabrication of perovskite thin film applied for X-ray detection, and the main reason is the lower X-ray attenuation ability of perovskite thin film than that of perovskite SCs. The general method for preparing perovskite thin film is the spin-coating process. Yang et al. [32] reported that a 700 nm MAPbI$_3$ thin film can only survive under a high bias of 5 V for 15 min. However, the X-ray detector based on the MAPbI$_3$ thin film shows a normal sensitivity of 2.48×10^{-2} μC·Gy$_{air}^{-1}$·cm^{-2}. Basiricò et al. [42] reported triple-cation perovskite (Cs$_{0.05}$FA$_{0.79}$MA$_{0.16}$Pb(I$_{0.8}$ Br$_{0.2}$)$_3$) thin films applied in an X-ray detector, which presented a sensitivity 3.7 ± 0.1 μC·Gy^{-1}·cm^{-2} without bias. The good device performance is ascribed to two major factors: (i) high mobility-lifetime (μτ) product in the triple-cation perovskite due to a low degree of disorder, and (ii) efficient electron and hole transport due to ambipolar charge transport in the triple-cation perovskite. Mixing n-type iodide with p-type bromide in the perovskites provides high electron and hole mobilities that grant an efficient charge collection and a fast detection response for the device. In addition, there are also some novel production methods to fabricate the perovskite. Possanzini et al. [43] reported fully textile perovskite-based direct X-ray detectors, in which the photoactive layer was constituted by a silk satin fabric functionalized with MAPbBr$_3$. Sensitivity values up to 12.2 ± 0.6 μC·Gy^{-1}·cm^{-2} and a limit of detection down to 3×10^3 nGy$_{air}$·s^{-1} were achieved.

3.1.2. Inorganic 3D ABX$_3$ Structure

Single Crystals (SCs)

CsPbBr$_3$ perovskite has high X-ray attenuation ability, a highly effective atomic number, high resistance and better long-term stability than the organic counterpart. These advantages attracted many researchers' attention to boost the development of CsPbBr$_3$-based X-ray detectors. Fan et al. [44] applied a hole extraction layer of MoO$_3$ on the CsPbBr$_3$

photoactive layer to increase the hole carrier collection in the X-ray detector and improve its signal current under the X-ray radiation. The sensitivity of X-ray detectors after covering the MoO_3 layer can reach up to 2552 $\mu C \cdot Gy_{air}^{-1} \cdot cm^{-2}$ under an electric field of 45 $V \cdot cm^{-1}$. Zhang et al. [45] prepared $CsPbBr_3$ perovskite by a low-temperature solution method, which exhibited high transmittance and large mobility-lifetime products for the X-ray detector with an asymmetric electrode configuration, and the ion migration in the device was effectively suppressed even under a high voltage. The device sensitivity achieved 1256 $\mu C \cdot Gy_{air}^{-1} \cdot cm^{-2}$ for 80 kVp X-ray radiation under an electric field of 20 $V \cdot mm^{-1}$. Peng et al. [46] developed a low-temperature crystallization strategy to grow $CsPbBr_3$ SCs in water. The hole and electron mobilities of $CsPbBr_3$ SCs reached 128 and 160 $cm^2 \cdot V^{-1} \cdot s^{-1}$, respectively. Finally, the device using $CsPbBr_3$ SCs showed a high X-ray sensitivity of 4086 $\mu C \cdot Gy_{air}^{-1} \cdot cm^{-2}$.

Other Structures

Other structures of $CsPbBr_3$, such as nanocrystals [47], microcrystals [48,49], quasi-monocrystals [23] and thin films [50], have been developed for X-ray detectors. Gou et al. [48] achieved a self-powered X-ray detector based on a microcrystalline $CsPbBr_3$ thick film by the solution process. A sensitivity of 470 $\mu C \cdot Gy_{air}^{-1} \cdot cm^{-2}$ was obtained for the X-ray photodetector under a low dose rate 0.053 $\mu Gy_{air} \cdot s^{-1}$ without bias. Matt et al. [49] employed the melting process to fabricate $CsPbBr_3$ microcrystals that showed high crystallinity and chemical purity. The film featured a resistance of 8.5 $G\Omega$ cm and a hole mobility of 18 $cm^2 \cdot V^{-1} \cdot s^{-1}$. The corresponding device showed a sensitivity of 1450 $\mu C \cdot Gy_{air}^{-1} \cdot cm^{-2}$ under an electric field of 1.2×10^4 $V \cdot cm^{-1}$ and a detection limit below $\mu Gy_{air} \cdot s^{-1}$. Pan et al. [23] used a hot-pressing method to produce thick quasi-monocrystalline $CsPbBr_3$ films with uniform crystalline orientations. They mentioned that the high crystalline quality of the $CsPbBr_3$ films and the self-formed shallow bromide vacancy defects during the high-temperature process result in a large $\mu\tau$ product. The X-ray detector using thick quasi-monocrystalline $CsPbBr_3$ films shows a sensitivity of 55,684 $\mu C \cdot Gy_{air}^{-1} \cdot cm^{-2}$, surpassing the sensitivity of all other perovskite-based X-ray detectors. A recorded sensitivity was achieved for the perovskite-based X-ray detector made by the all-vacuum deposition process. Lai et al. [50] demonstrated a perovskite-based X-ray detector with a p–i–n heterojunction, in which the Cs-based perovskite active layer was fabricated by vacuum deposition. The self-powered X-ray detector showed an efficient charge collection, an exceptionally high X-ray sensitivity of 1.2 $C \cdot Gy_{air}^{-1} \cdot cm^{-3}$ and a low detection limit of 25.69 $nGy_{air} \cdot s^{-1}$ under zero-bias conditions. Moreover, the volume sensitivity ($C \cdot Gy_{air}^{-1} \cdot cm^{-3}$) was only one-fifth of that of the vacuum-deposited $CsPbI_2Br$ devices.

3.2. Low-Dimensional Perovskite Materials

Low-dimensional perovskite materials are mostly used in light sensors and LEDs [51]. Low-dimensional perovskite material is characterized by a layered crystal structure, in which the corner-sharing BX_6 octahedra are separated between two spacers of large-sized $R-NH_3^+$ cations. The structural formula of low-dimensional layered perovskite can be presented as $(R-NH_3)_2A_{n-1}B_nX_{3n+1}$ (Ruddlesden–Popper phase). When n is equal to 1, a basic two-dimensional layered perovskite with a formula of $(R-NH_3)_2BX_4$ is obtained. By controlling the layer number n of BX_6 octahedra, a variety of low-dimensional perovskite materials are formed. When the layer number of BX_6 octahedra is close to infinity, the two-dimensional layered perovskite can convert into a three-dimensional perovskite. In the two-dimensional layered perovskite, the carrier transport is limited within the layered BX_6 octahedra and leads to anisotropic carrier transport because of a strong dielectric difference and a weak bonding between the large-sized $R-NH_3^+$ and the inorganic BX_6 octahedra. A low dark current of the X-ray detector based on the low-dimensional perovskite is achieved due to suppressed ion migration and large E_g [52].

3.2.1. Two-Dimensional (2D) Perovskite Materials

The architecture and material properties of two-dimensional (2D) perovskite materials as well as their advantages were briefly introduced. Next, the recent research on the application of two-dimensional materials in X-ray sensing devices is summarized.

Single Crystal

Li et al. [53] used a 2D perovskite of (F-PEA)$_2$PbI$_4$ (F-PEA: fluorophenethyl) material as the active layer for the hard X-ray detector. Adding the fluorine atoms in the large-sized cation can strengthen the interaction between the fluorine atom and the benzene ring, which improves the stability, effectively suppresses the ion migration and reduces the dark current of the X-ray detector. Figure 2a is the structural architecture of the device. The device sensitivity under 120 kV$_p$ hard X-ray irradiation is 3402 μC·Gy$^{-1}_{air}$·cm^{-2} and its detection limit is 23 nGy$_{air}$·s^{-1}, as shown in Figure 2b and Figure 2c, respectively. Qian et al. [54] synthesized a 2D (PMA)$_2$PbI$_4$ single crystal and used the ion implantation to implant copper ions into the 2D perovskite (refer to Figure 2d). The quantum confinement effect of 2D layered perovskite can effectively suppress the dark current of the X-ray detector. The device sensitivity under the X-ray irradiation is 283 μC·Gy$_{air}^{-1}$·cm^{-2} and its detection limit is 2.13 μGy$_{air}$·s^{-1}, as shown in Figure 2e and Figure 2f, respectively.
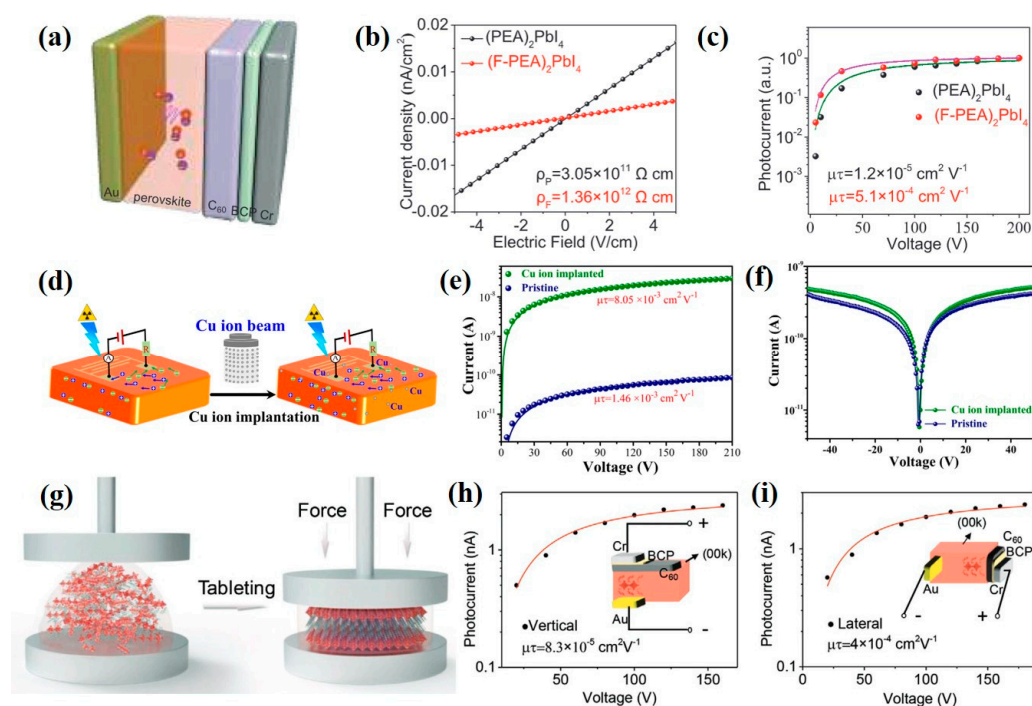

Figure 2. (**a**) Device structure, (**b**) dark current density and (**c**) photocurrent of self-powered X-ray detector based on 2D (F-PEA)$_2$PbI$_4$ perovskite [53]. (**d**) Schematic diagram of Cu ion implantation on the (PMA)$_2$PbI$_4$-based X-ray detector. (**e**) Sensitivity and (**f**) detection limit of (PMA)$_2$PbI$_4$-based X-ray detector after ion implantation [54]. (**g**) Schematic diagram of tableting process for the (F-PEA)$_3$BiI$_6$ SCs. Photocurrent of X-ray detector using (F-PEA)$_3$BiI$_6$ single crystal under (**h**) vertical and (**i**) horizontal electric fields [55].

Li et al. [55] fabricated a single crystal of (F-PEA)$_3$BiI$_6$ by pressing disordered two-dimensional perovskite powders into thick films with ordered single-crystal structures under high pressure. Figure 2g is the process of pressure tableting. Strong bonding energy between bismuth ions (Bi^{3+}) and iodine ions (I$^-$) can effectively prevent ion migration and reduce the dark current of the X-ray detector. The device detection limit is 30 nGy$_{air}$·s^{-1} and the electrical detection of different crystal orientations is compared in Figure 2h,i.

Film

Ledee et al. [51] deposited 2D layered perovskite of PEA_2PbBr_4 ($PEA = C_6H_5C_2H_4NH^{3+}$) on a PET flexible substrate coated with interdigitated electrodes, and such a device structure works as a photoconductor, as shown in Figure 3a. The channel width and length of finger electrodes were designed as 7.56 mm and 20 μm, respectively, to assist the layered arrangement of 2D material and effectively collect the charge carriers. As shown in Figure 3b, when the dose rate increases, the sensitivity of X-ray detectors decreases. The sensitivity is calculated as the first derivative of photocurrent with respect to the dose rate and it is normalized by the total pixel area of 0.63 mm^2. The device under X-ray irradiation of 150 kVp presented a sensitivity of 806 $\mu C \cdot Gy_{air}^{-1} \cdot cm^{-2}$. Figure 3c shows the SNR as a function of dose rate. When the SNR of the X-ray detector is equal to 3, the corresponding detection limit reaches a low value of 42 $nGy_{air} \cdot s^{-1}$.

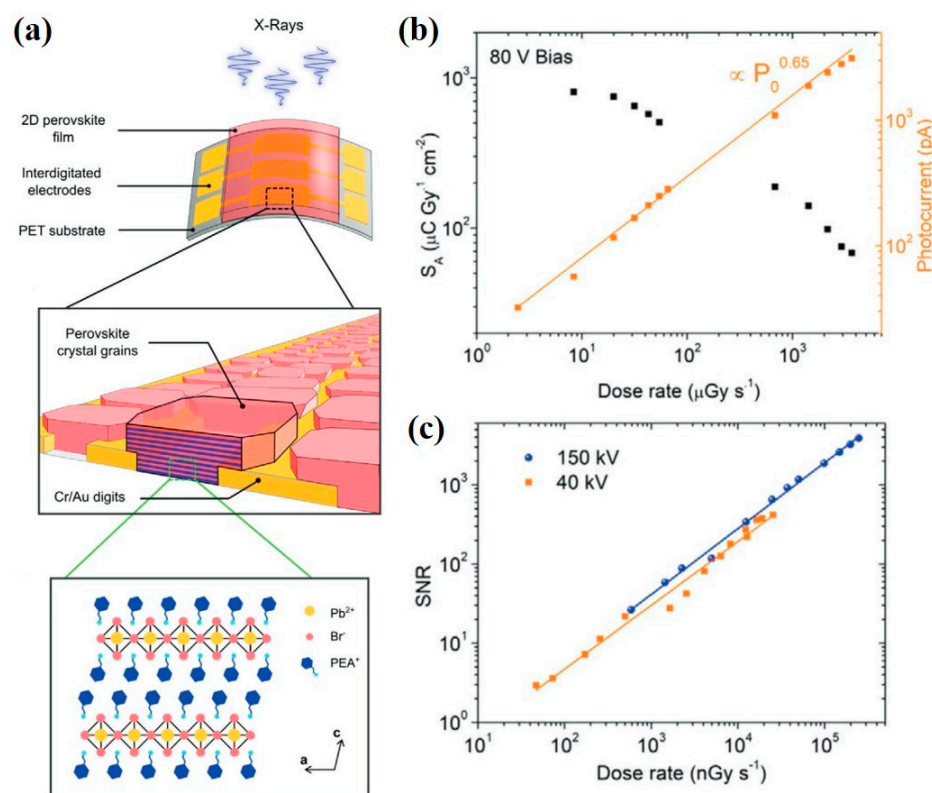**Figure 3.** (**a**) Photoconductor-type X-ray detectors by deposition of 2D PEA_2PbBr_4 micro-crystalline films on a flexible PET substrate. (**b**) Sensitivity per unit area (S_A, black curve) and photocurrent (orange curve) as a function of dose rate. (**c**) SNR as a function of dose rate for the device under 150 kVp (blue curve) and 40 kVp (orange curve) accelerating voltages [51].

Compared with the single crystal, the perovskite film has more defects, which results in increased dark current in the X-ray detector and thereby decreased device sensitivity. Due to the large-sized cation in the 2D perovskite, the ion migration can be inhibited to reduce the dark current of the device. However, the 2D perovskite has a poor light response to X-rays due to anisotropic charge transport. As a result, the device applying 2D perovskite delivers an inferior sensitivity compared to the 3D counterpart.

3.2.2. Quasi-2D Perovskite Materials

Ji et al. [56] produced a quasi-2D $BA_2EA_2Pb_3Br_{10}$ (BA: $C_4H_9NH_3$; EA: $C_2H_5NH_3$) perovskite as an X-ray absorber for the X-ray detector, and they utilized spontaneous ferroelectric polarization (Ps) to effectively separate the photoinduced carriers and facilitate their transport for better X-ray sensitivity, as shown in Figure 4a,b. Tsai et al. [57] used the 2D layered perovskite of $(BA)_2(MA)_2Pb_3I_{10}$ as the active layer material in an X-ray detector

for converting X-rays into charges, and the device sensitivity reached $0.276 \ C \cdot Gy_{air}^{-1} \cdot cm^{-3}$, as shown in Figure 4c,d. In addition, Tsai et al. [58] also introduced *n*-butylamine iodide in the methylammonium lead iodide precursor to prepare a quasi-2D layered perovskite, as shown in Figure 4e. The corresponding device showed a stable performance for a detection time of more than 15 h, and the X-ray sensitivity of the device was $1214 \ \mu C \cdot Gy_{air}^{-1} \cdot cm^{-2}$, as shown in Figure 4f.
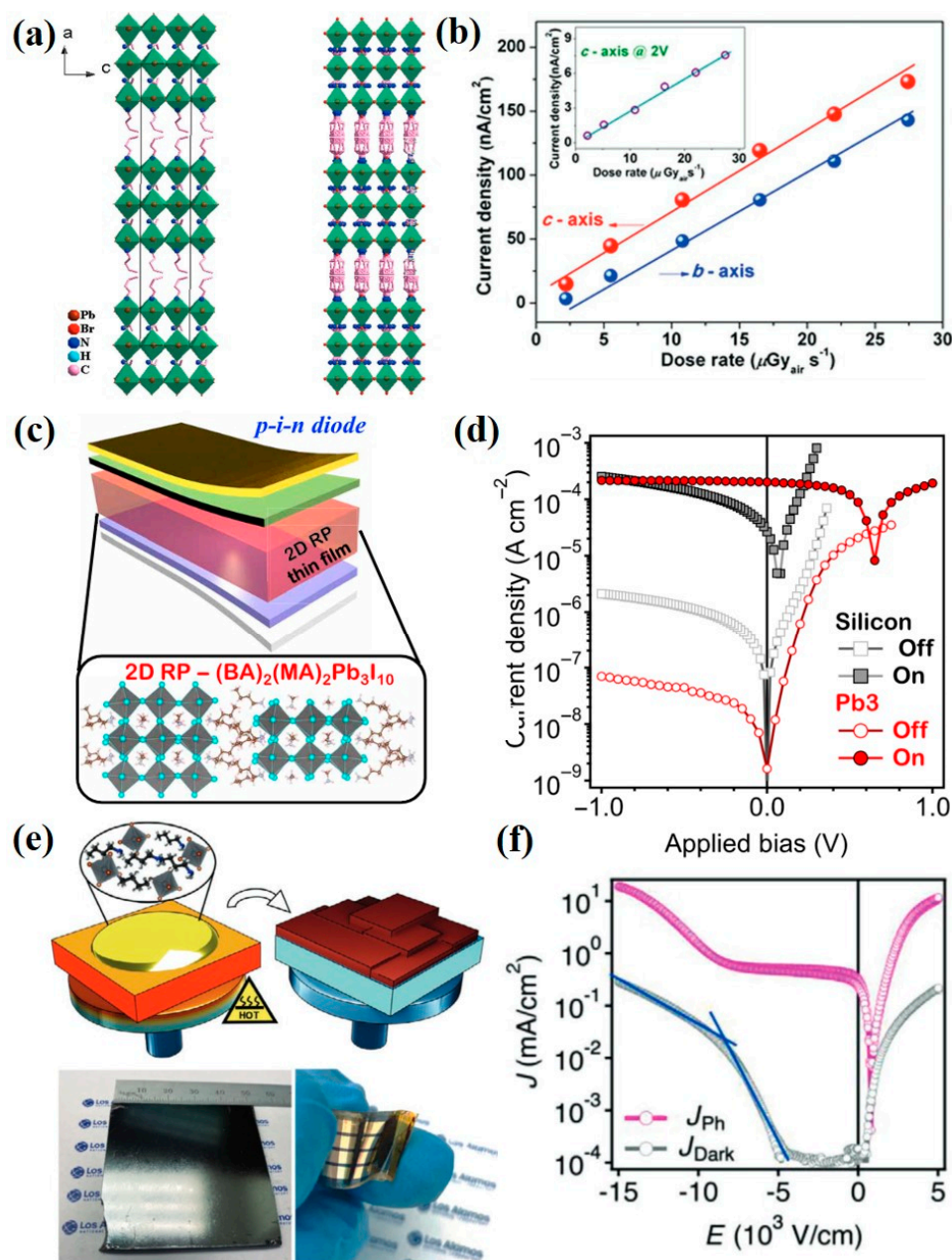
Figure 4. (**a**) Crystal structure of the quasi-2D $BA_2EA_2Pb_3Br_{10}$ perovskite. (**b**) X-ray-generated photocurrent of $BA_2EA_2Pb_3Br_{10}$ perovskite at various dose rates at a bias of 10 V [56]. (**c**) A p–i–n device architecture and (**d**) J–V curve of X-ray detector based on quasi-2D $(BA)_2(MA)_2Pb_3I_{10}$ perovskite [57]. (**e**) Fabrication process of thick film growth of quasi-2D perovskite and (**f**) J–V curve of corresponding X-ray detector [58].

3.2.3. One-Dimensional (1D) Perovskite Materials

Zhang et al. [59] synthesized a 1D inorganic perovskite of $CsPbI_3$ as an absorbing material for the conversion of X-ray photons into charge carriers, and the $CsPbI_3$-based

device had a high bulk resistivity of 7.4×10^9 $\Omega \cdot$cm, a large mobility–lifetime product of 3.63×10^{-3} $cm^2 \cdot V^{-1}$ and X-ray sensitivity of 2.37 $mC \cdot Gy^{-1} \cdot cm^{-2}$.

3.2.4. Zero-Dimensional (0D) Perovskite Materials

Unlike the traditional 3D perovskite structures with corner-sharing BX_6 octahedra, deficient perovskite has isolated BX_6 octahedra, which results in a zero-dimensional (0D) perovskite structure. Xu et al. [60] used electrostatic-assisted spray coating to fabricate the all-inorganic 0D perovskite material of Cs_2TeI_6 with a large area for the X-ray detector. Figure 5a is the schematic illustration of the spraying process for preparing the Cs_2TeI_6 perovskite, and the device structure of the X-ray detector is composed of $FTO/TiO_2/Cs_2TeI_6/PTAA/Au$ (refer to the inset in Figure 5b). Under X-ray irradiation of 40 kVp and an electric field of 250 $V \cdot cm^{-1}$, the device sensitivity was 19.2 $\mu C \cdot Gy_{air}^{-1} cm^{-2}$. Figure 5b compares the X-ray attenuation efficiency of different active materials, including CdTe, a-Se and Cs_2TeI_6, with different thicknesses, indicating that the Cs_2TeI_6 perovskite exhibits a comparable X-ray attenuation efficiency to CdTe. Xu et al. [61] used the 0D single crystal of Cs_4PbI_6 perovskite to make an X-ray detection device, and its mobility–lifetime product ($\mu\tau$) reached 9.7×10^{-4} $cm^2 \cdot V^{-1}$. Figure 5c shows the J–V curves of the fabricated device with different exposure dose rates and the resultant sensitivity of the device was 451.49 $\mu C \cdot Gy_{air}^{-1} \cdot cm^{-2}$ at an operating bias of 30 V, as seen in Figure 5d.
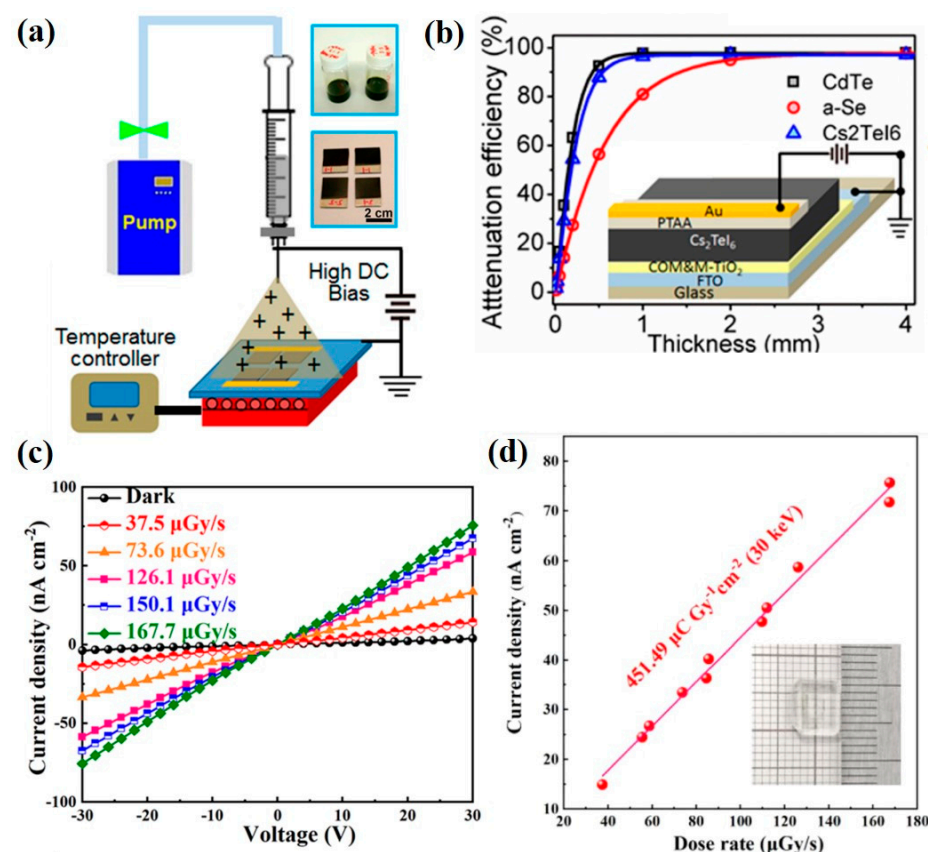

Figure 5. (**a**) Schematic illustration of electrostatic-assisted spray coating process for deposition of large-area Cs_2TeI_6 perovskite. (**b**) Comparison of attenuation efficiency of CdTe, a-Se and Cs_2TeI_6 with different thicknesses for X-ray irradiation. Inset illustrates the device structure [60]. (**c**) J–V curves and (**d**) photocurrent as a function of dose rate of X-ray detector using Cs_4PbI_6 single crystal [61].

3.3. $A_2B_2X_6$ Double-Perovskite Materials

Inorganic $Cs_2AgBiBr_6$ double perovskite is the most popular material in the field of X-ray detection, and its advantages include elements with a large Z number, such as Ag and Bi, which have a high X-ray attenuation ability. When a large electric field is applied to the

$Cs_2AgBiBr_6$-based X-ray detector, the $Cs_2AgBiBr_6$ double perovskite is durable. Moreover, the ion migration in the X-ray detector is inhibited to lower the dark current.

Steele et al. [62] used $Cs_2AgBiBr_6$ double perovskite for X-ray detection. The device architecture was composed of $Au/Cs_2AgBiBr_6/Au$ stacking structure and its sensitivity to X-ray irradiation reached 105 $\mu C \cdot Gy_{air}^{-1} \cdot cm^{-2}$, as shown in Figure 6a. In the research demonstrated by Pan et al. [63], they reduced the disordered arrangement of Ag^+ and Bi^{3+} ions in the $Cs_2AgBiBr_6$ double perovskite through the control of thermal annealing and surface treatment, which increases the bulk resistivity of perovskite and reduces the dark current. It is indicated that this $Cs_2AgBiBr_6$ SC is a p-type semiconductor to facilitate hole transport.
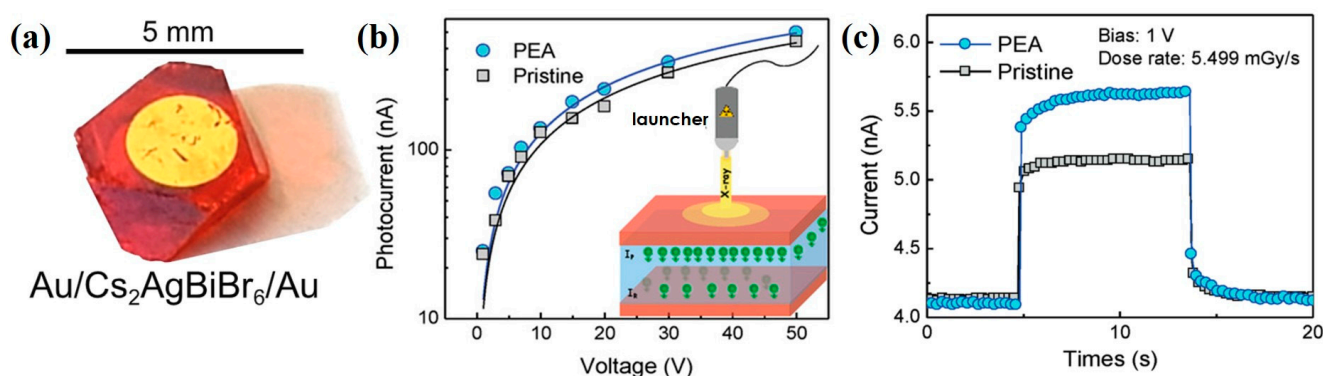

Figure 6. (**a**) Photo of X-ray detector with a device architecture of $Au/Cs_2AgBiBr_6$ perovskite/Au [62]. (**b**) I–V curves of X-ray detectors using pristine $Cs_2AgBiBr_6$ and PEA-$Cs_2AgBiBr_6$ single-crystal. (**c**) X-ray response of the $Cs_2AgBiBr_6$- and PEA-$Cs_2AgBiBr_6$-based devices [64].

Yuan et al. [64] proposed that phenethylamine bromide (PEABr) can strengthen the molecular arrangement in the $Cs_2AgBiBr_6$ perovskite and were able to in situ tune the order–disorder phase transition in the $Cs_2AgBiBr_6$ single crystals. Additionally, the improvement of ordering extent can effectively reduce the defect density of perovskite material and improve carrier mobility. These PEA-$Cs_2AgBiBr_6$ crystals were utilized in the application of X-ray detection. The working mechanism is shown in Figure 6b. The PEA-$Cs_2AgBiBr_6$-based device showed an enhanced X-ray response due to the improvement of carrier mobility, as shown in Figure 6c, and the sensitivity of the PEA-$Cs_2AgBiBr_6$-based X-ray detector was 288.8 $\mu C \cdot Gy_{air}^{-1} \cdot cm^{-2}$.

3.4. $A_3B_2X_9$ Lead-Free Perovskite Materials

Lead-free perovskite with a vacancy-ordered structure of $A_3B_2X_9$ (A: Cs^+, Rb^+, NH_4^+; M: Bi^{3+}, Sb^{3+}; X: Br^-, I^-) is a potential candidate for X-ray detectors due to its eco-friendly composition and high attenuation coefficient to X-ray irradiation. This perovskite has an equivalent composition of $AB_{2/3}X_3$ that indicates that one in three octahedral B^{3+}-sites is occupied by a vacancy for maintaining charge neutrality. These materials exhibit a layered structure as 2D layered perovskite derivatives. This perovskite contains heavy elements with a large Z number to deliver a high attenuation capability to X-ray irradiation based on the relationship $\alpha \propto Z^4/E_{ph}^3$. The application of vacancy-ordered perovskite for X-ray detectors is introduced in this section.

Zhuang et al. [65] used a 2D layered perovskite single crystal of $(NH_4)_3Bi_2I_9$ for the X-ray detector. Due to its inherent 2D layered structure, ion migration in the $(NH_4)_3Bi_2I_9$ perovskite can be suppressed. The as-fabricated device presented a low detection limit of 55 $nGy_{air} \cdot s^{-1}$ and exhibited a good X-ray attenuation performance due to the presence of the heavy element Bi. Dong et al. [66] applied the $MA_3Bi_2I_9$ perovskite for the direct-conversion X-ray detector. They used the blade-coating method to deposit the perovskite film onto the ITO substrate and added the MACl additive to slow down the crystal growth rate to reduce pinholes in the blade-coated perovskite film. The X-

ray sensitivity and the detection limit of the device were 100.16 $\mu C \cdot Gy_{air}^{-1} \cdot cm^{-2}$ and 98.4 $nGy_{air} \cdot s^{-1}$, respectively. Li et al. [67] synthesized a single-crystal, low-dimensional $FA_3Bi_2I_9$ perovskite material as the X-ray absorber for an X-ray detector. Figure 7a shows the solution-processed method for the fabrication of the $FA_3Bi_2I_9$ single crystal. The device had a high bulk resistivity of $7.8 \times 10^{10} \Omega \cdot cm$, and the X-ray detection limit and the sensitivity of the device were 200 $nGy_{air} \cdot s^{-1}$ and 598.1 $\mu C \cdot Gy_{air}^{-1} \cdot cm^{-2}$, respectively. Since the stability of the device is severely affected by the organic cations, Zhang et al. [68] synthesized an all-inorganic low-dimensional perovskite of $Cs_3Bi_2I_9$ single crystal as the active layer for X-ray sensing. The $Cs_3Bi_2I_9$ single crystal was formed by the solution method and then made into the X-ray sensing device, as shown in Figure 7b. The sensitivity and the detection limit of the device for X-ray sensing reached 1652.3 $\mu C \cdot Gy_{air}^{-1} \cdot cm^{-2}$ and 130 $nGy_{air} \cdot s^{-1}$, respectively.

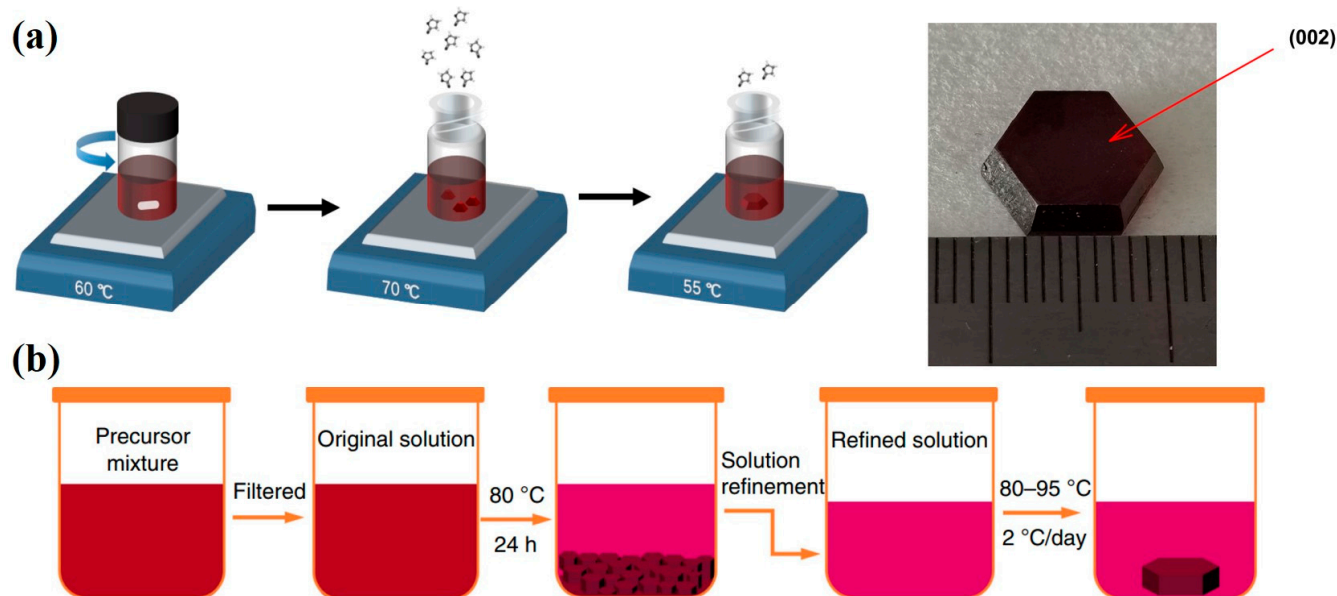**Figure 7.** (**a**) $FA_3Bi_2I_9$ single crystal synthesized by the solution method through controlling the growth mechanism [67]. (**b**) Schematic diagram of preparation of the $Cs_3Bi_2I_9$ single crystals by the nucleation-controlled solution method [68].

According to the X-ray absorption mechanism, the active layer with heavy elements has high absorption of X-ray irradiation. Therefore, X-ray detectors using perovskite materials with heavy metal elements of bismuth have good sensitivity to X-ray irradiation. Compared with the organic–inorganic hybrid perovskites, the inorganic perovskites present superior resistance to moisture, so the inorganic $Cs_3Bi_2I_9$ is a suitable material for X-ray sensing.

3.5. Large-Area Perovskite X-ray Detectors

To make the perovskite-based X-ray detector able to directly take 2D images, a large area of perovskite layers, greater than 100 cm^2, is favorable for the integration on the commercial thin-film transistor array; therefore, a scalable deposition process for the perovskite active layer in the X-ray detector is necessary. In this section, we summarize the large-area deposition process of perovskite active layers for the manufacture of perovskite-based X-ray detectors and their performance under X-ray irradiation.

Many large-area deposition processes of perovskite active layers, such as inkjet printing, doctor blade coating, spray coating, etc., have been demonstrated. Mescher et al. [69] reported a direct-conversion X-ray detector, in which the perovskite film was inkjet-printed onto flexible substrates, as shown in Figure 8a. The as-fabricated device achieved a sensitivity of 59.9 $\mu C \cdot Gy_{air}^{-1} \cdot cm^{-2}$ at a low external voltage (0.1 V) with 70 kV_p X-ray irradiation. Liu et al. [70] demonstrated an X-ray detector via a low-cost ink-printed coating

of CsPbBr$_3$ quantum dots on a flexible substrate, as shown in Figure 8b. A sensitivity of 1450 μC·Gy$_{air}^{-1}$·cm^{-2} for the X-ray detector was obtained when the device was exposed to a low exposure dose rate of about 17.2 μGy$_{air}$·s^{-1} under a bias voltage of 0.1 V. Li et al. [71] demonstrated a hybrid X-ray detector with Cs$_2$AgBiBr$_6$ and (C$_{38}$H$_{34}$P$_2$)MnBr$_4$ scintillators synthesized by the tablet-pressing method, as shown in Figure 8c. The addition of a (C$_{38}$H$_{34}$P$_2$)MnBr$_4$ scintillator in the X-ray detector could suppress the ion migration of Cs$_2$AgBiBr$_6$ perovskite to reduce the dark current and increase the carrier collection efficiency. The final device achieved a sensitivity of 114 μC·Gy$_{air}^{-1}$·cm^{-2} and a low detection limit of 200 nGy$_{air}$·s^{-1} under a hard X-ray exposure of 120 kV$_p$. Ciavatti et al. [72] introduced a bar-coated perovskite for the direct-conversion X-ray detector with a sensitivity of 494 μC·Gy$_{air}^{-1}$·cm^{-2} at 150 kV$_p$ X-ray irradiation under a low operating voltage of less than 4 V, as shown in Figure 8d. Guo et al. [73] provided a facile mobile-platform-assisted electrospray method for the preparation of perovskite films with a large area of 100 cm^2 on flexible substrates. By adjusting the spraying parameters, it is possible to control the growth orientation of Cs$_2$TeI$_6$ perovskite. The Cs$_2$TeI$_6$-based X-ray detector, in which the perovskite shows a preferred crystalline orientation of (222) facet, achieves a resistivity of 1.9 × 10^{11} Ω·cm and a sensitivity of 226.8 μC·Gy$_{air}^{-1}$·cm^{-2}, as shown in Figure 8e. Kim et al. [22] used doctor blade coating to deposit a polycrystalline MAPbI$_3$ thick film onto large-area thin-film transistor (TFT) substrates. This is the first work to directly deposit the MAPbI$_3$ perovskite on a large-area TFT substrate. The device achieves a sensitivity of up to 1.1 × 10^4 μC·Gy$_{air}^{-1}$·cm^{-2} under irradiation from a 100 kV$_p$ X-ray source, which is higher than that of current X-ray detectors using amorphous selenium or thallium iodide. They adjusted the charge injection interface to reduce the dark current by overlaying two additional polymer/perovskite composites on the upper and lower interfaces of 830 μm thick MAPbI$_3$. Yang et al. [74] proposed an aerosol–liquid–solid (ALS) process to prepare mixed halide perovskite thick films for direct-conversion X-ray detectors. The ALS process can produce high-quality perovskite films of different compositions on conductive glass substrates or TFT substrates and facilitate the vertical growth of perovskite grains without grain boundaries. Such a columnar perovskite grain significantly improves the carrier transport across the perovskite film. The X-ray detector with a CsPbI$_2$Br thick film achieves a sensitivity of 1.48 × 10^5 μC·Gy$_{air}^{-1}$·cm^{-2} and a low detection limit of 280 nGy$_{air}$·s^{-1}, as shown in Figure 8f. The authors further demonstrated the high-resolution imaging capability, good stability, and strong resistance to X-ray radiation damage for the CsPbI$_2$Br-based X-ray detector.
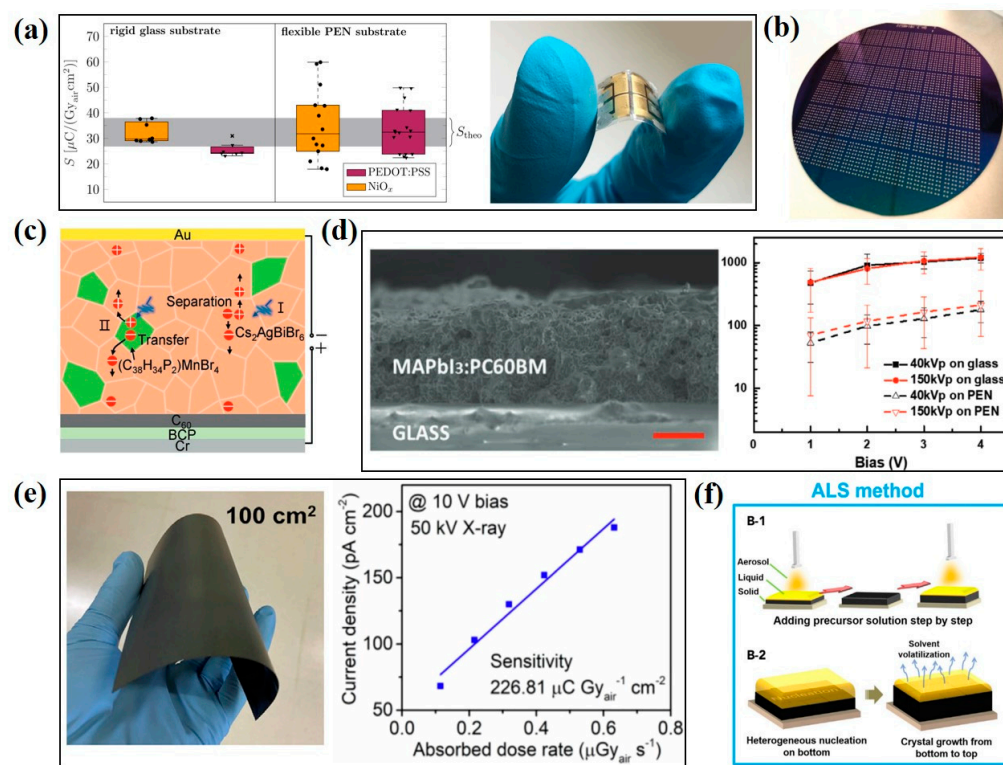
Figure 8. Application of large-area perovskite film for X-ray detectors. (**a**) Reliability of sensitivity for X-ray detectors fabricated on rigid and flexible substrates [69]. (**b**) Photo of large-area $CsPbBr_3$ quantum dots deposited on TFT array [70]. (**c**) Illustration of working principle of X-ray detector using mixed $Cs_2AgBiBr_6/(C_{36}H_{34}P_2)MnBr_4$ scintillator [71]. (**d**) Cross-sectional SEM and X-ray photo-response of the device with bar coating of $MAPbI_3$:PC60BM mixed absorber [72]. (**e**) Large-area lead-free Cs_2TeI_6 perovskite fabricated by electro-spraying on flexible substrates and the relationship between the photocurrent density of Cs_2TeI_6-based device and the exposure dose rate [73]. (**f**) Schematic illustration of the perovskite layer prepared by the ALS process [74].

4. Conclusions and Outlook

In recent years, many researchers have proposed to replace the commonly used a-Se with perovskite material as the absorber layer for X-ray detectors because of its excellent X-ray attenuation ratio, long carrier lifetime, high defect tolerance and long electron–hole drift length. Compared to an a-Se absorber layer, using emerging perovskite materials in an X-ray detector can provide better X-ray detection performance at a lower cost and with less environmental pollution. At the early stage in the development of perovskite-based X-ray detectors, single-crystal perovskite was used to replace a-Se in X-ray detectors and showed good performance in response to X-ray irradiation due to its high crystalline quality, smooth morphology, high bulk resistivity, low trap density and sufficient thickness to attenuate X-rays. Polycrystalline perovskite-based X-ray detectors show poorer performance than their single-crystalline counterparts because of the increased grain boundary. However, their fabrication methods have the potential for the mass production of thick perovskite films for large-area X-ray detectors. Organic–inorganic hybrid perovskite materials, such as $MAPbI_3$ and $MAPbBr_3$, are commonly used as absorbers for X-ray detectors, and their application in X-ray detectors shows good performance under X-ray irradiation. However, their environmental stability is a major challenge due to the rapid degradation of perovskite upon exposure to humidity, heat, light and oxygen. All inorganic perovskite materials, such as $CsPbBr_3$, show better environmental stability than organic–inorganic perovskite, and the X-ray detectors with inorganic perovskite still have high X-ray sensitivity. The introduction of large-sized cations in the 3D perovskite separates the 3D perovskite into the 2D layered perovskite. The anisotropic carrier transport in the 2D layered perovskite

can inhibit ion migration to reduce the dark current of the device but decrease the device's performance in response to X-ray irradiation. As a result, the sensitivity of X-ray detectors using 2D perovskite is generally lower than that of their 3D perovskite counterparts. Quasi-2D perovskite material ($n > 1$) such as $BA_2EA_2Pb_3Br_{10}$ has a better response to X-rays than the pure 2D materials ($n = 1$) and still has good stability. After a long period of measurement, the X-ray detectors based on quasi-2D perovskite still maintain a very stable performance. The application of a 1D inorganic perovskite nanorod, such as $CsPbI_3$, in the X-ray detector shows a high X-ray sensitivity owing to its high resistivity and large carrier mobility–lifetime product. The 0D all-inorganic perovskite material of Cs_2TeI_6 is demonstrated as a potential candidate for the X-ray detector by virtue of its high X-ray sensitivity and environmental stability. Double-perovskite materials, such as $Cs_2AgBiBr_6$, contain the large Z-numbered elements of Ag and Bi, which have a better ability to attenuate X-ray irradiation. Its stable crystal structure can effectively inhibit ion migration in the device under a bias voltage; therefore, the corresponding device has a low dark current. Lead-free perovskite materials with a composition formula of $A_3B_2X_9$ (e.g., $MA_3Bi_2I_9$ and $Cs_3Bi_2I_9$), in which the Pb atoms are replaced with larger Z-numbered Bi atoms, show the advantages of high attenuation of X-rays and eco-friendly properties. These properties make such materials promising as active layers in X-ray sensing devices. Furthermore, all inorganic lead-free perovskite materials exhibit high resistance to moisture, so they are suitable candidates for X-ray detectors. The key device parameters of perovskite-based X-ray detectors are summarized in Table 1.

To meet the commercial requirements for flat panel X-ray detectors, direct deposition of a perovskite layer with an area larger than 100 cm^2 on the thin-film transistor array is necessary. Large-area fabrication methods for preparing the thick perovskite film, such as inkjet printing, doctor blade coating, spray coating and the ALS process, are utilized to fabricate large-area perovskite-based X-ray detectors. The large-area fabrication methods with a low-temperature process can further deposit a perovskite thick film onto the flexible substrates or TFT modules. The improvement of perovskite film quality, film uniformity and composition uniformity are the major challenges for large-area perovskite film. The as-prepared perovskite thick film by these processes is a polycrystalline film that has abundant grain boundaries and defects to trap the photogenerated carriers and further reduce the X-ray detector performance. By optimizing the experimental parameters and precisely controlling the environment during the deposition of perovskite film, a large-area perovskite thick film with large grain size, uniform film morphology and composition and fewer defects can be obtained. In conclusion, it is worth devoting more efforts toward developing facile, low-cost and eco-friendly fabrication methods for the preparation of large-area, durable, uniform, highly sensitive, low-detection-limit and low-toxicity perovskite films for X-ray detection.

Table 1. Summary of key parameters of perovskite-based X-ray detectors.

Crystal Structure	Materials	Crystal Type	Growth Method	Thickness (mm)	E (V·mm^{-1})	$\mu\tau$ (cm^2·V^{-1})	S (μC·Gy$_{air}$$^{-1}$·cm^{-2})	LoD (nGy$_{air}$·s^{-1})	Ref.
ABX$_3$ (Organic)	MAPbI$_3$	Single crystals	ITC	NA	100	NA	700,000	1.5	[31]
	MAPbI$_3$	Single crystals	ITC	NA	10	1.6×10^{-3}	NA	NA	[32]
	MAPbI$_3$	Single crystals	ITC	1.2 ± 0.04	NA	5.3×10^{-3}	3.67×10^3	80.6	[33]
	DMAMAPbI$_3$	Single crystals	ITC	1.2 ± 0.04	NA	7.2×10^{-3}	1.18×10^4	16.9	[33]
	GAMAPbI$_3$	Single crystals	ITC	1.2 ± 0.04	NA	1.3×10^{-2}	2.31×10^4	16.9	[33]
	MAPbI$_3$	Single crystals	Solution	1	NA	1.49×10^{-3}	968.9	NA	[34]
	MAPbI$_3$	Single crystals	Solution	2~3	3.3	2.57×10^{-3}	1471.1	46,000	[35]
	MAPbI$_3$	Polycrystals (wafer)	Sintering process	0.2~1	200	2×10^{-4}	2527	NA	[36]
	MAPbBr$_3$	Single crystals	ITC	NA	0.83	4.1×10^{-2}	259.9	NA	[37]
	MAPbBr$_3$	Single crystals	Solution	NA	1.43×10^4	NA	359	22,100	[38]
	MAPbBr$_3$	Single crystals	Fully textile	0.05	17	NA	12.2 ± 0.6	3000 (for stacked)/8000 (for planar)	[43]
	Bi^{3+}-doped MAPbBr$_3$	Single crystals	Solution	1.68	31.5	4.12×10^{-4}	1.72×10^3	NA	[39]
	MA$_{0.6}$Cs$_{0.4}$PbBr$_3$	Single crystals	Solution	2	NA	4.64×10^2	2017	1200	[40]
	FA$_{0.85}$MA$_{0.1}$Cs$_{0.05}$Pb I$_{2.55}$Br$_{0.45}$	Single crystals	Thermal evaporation	1	-60	NA	$(3.5 \pm 0.2) \times 10^6$	NA	[41]
	Cs$_{0.05}$FA$_{0.79}$MA$_{0.16}$Pb (I$_{0.8}$Br$_{0.2}$)$_3$	Film	Spin coating	4.5×10^{-4}	200	NA	3.7 ± 0.1	NA	[42]

Table 1. *Cont.*

Crystal Structure	Materials	Crystal Type	Growth Method	Thickness (mm)	E ($V \cdot mm^{-1}$)	μτ ($cm^2 \cdot V^{-1}$)	S ($\mu C \cdot Gy_{air}^{-1} \cdot cm^{-2}$)	LoD ($nGy_{air} \cdot s^{-1}$)	Ref.
ABX$_3$ (Inorganic)	CsPbBr$_3$	Single crystals	Solution	NA	45	−NA	2552	20,900	[44]
	CsPbBr$_3$	Single crystals	Solution	1	20	$(2.5 \pm 0.2) \times 10^{-3}$	1256	NA	[45]
	CsPbBr$_3$	Single crystals	LTC	1	NA	NA	4086	NA	[46]
	CsPbBr$_3$	Microcrystals	Solution	0.018	0	NA	470	53	[48]
	CsPbBr$_3$	Microcrystals	Vitreous enamel	0.1	1.2×10^4	NA	1450	NA	[49]
	CsPbBr$_3$	Quasi-monocrystal	Hot pressing	0.24	4.2	1.32×10^{-2}	55,684	215	[23]
	CsPbI$_2$Br	Film	Co-evaporation	0.001	NA	NA	1.2×10^6	25.69	[50]
2D	(F-PEA)$_2$PbI$_4$	Single crystals	Solution	2	133	5.1×10^{-4}	3402	23	[53]
	(PMA)$_2$PbI$_4$	Single crystals	Cooling crystallization	0.9	NA	8.05×10^{-3}	283	2.13	[54]
	(F-PEA)$_3$BiI$_6$	Single crystals	Tablet pressing	NA	100	8.3×10^{-5}	118.6	30	[55]
	PEA$_2$PbBr$_4$	Film	Spin coating	$1.9 \pm 0.8 \times 10^{-3}$	500	$1.09 \pm 0.07 \times 10^{-5}$	806	42	[51]
Q-2D	BA$_2$EA$_2$Pb$_3$Br$_{10}$	Single crystals	Cooling crystallization	NA	20k	7.6×10^{-3}	6.8×10^3	5500	[56]
	BA$_2$EA$_2$Pb$_3$I$_{10}$	Film	Hot casting	4.70×10^{-4}	NA	NA	276,000	10,000	[57]
	MAPbI$_3$/n-butylamine iodide	Film	Spin coating	$2\text{–}3 \times 10^{-3}$	NA	NA	1214	NA	[58]
1D	CsPbI$_3$	Polycrystals	Solution	NA	NA	3.63×10^{-3}	2370	59.7	[59]
0D	Cs$_2$TeI$_6$	Polycrystals	E-spray deposition	0.5	250	5.2×10^{-5}	19.2	NA	[60]
	Cs$_4$PbI$_6$	Single crystals	Solution	NA	NA	9.7×10^{-4}	451.49	90	[61]
A$_2$B$_2$X$_6$	Cs$_2$AgBiBr$_6$	Single crystals	Solution	2	NA	NA	105	59.7	[62]
	Cs$_2$AgBiBr$_6$	Single crystals	Solution	2	25	NA	105	59.7	[63]
	Cs$_2$AgBiBr$_6$	Single crystals	Solution	2.2	22.7	NA	288	NA	[64]

Table 1. *Cont.*

Crystal Structure	Materials	Crystal Type	Growth Method	Thickness (mm)	E (V·mm^{-1})	uτ (cm^2·V^{-1})	S (μC·Gy$_{air}$$^{-1}$·cm^{-2})	LoD (nGy$_{air}$·s^{-1})	Ref.
A$_3$B$_2$X$_9$	MA$_3$Bi$_2$I$_9$	Film	Blade coating	50×10^{-3}	-3000 V cm^{-1}	9.7×10^{-6}	100.16	98.4	[66]
	FA$_3$Bi$_2$I$_9$	Single crystals	SSCE	0.9	NA	NA	598.1	0.2	[67]
	Cs$_3$Bi$_2$I$_9$	Single crystals	Solution	1.2	50	NA	1652.3	130	[68]
Large area process	MAPbI$_3$	Nanocrystals	Bar coating	10×10^{-3}	800	NA	2300	27,000	[72]
	MAPbI$_3$	Polycrystals	Doctor blade coating	0.83	10–240	1.5×10^{-4}	1.1×10^4	300	[22]
	CsPbBr$_3$	Monocrystal (quantum dot)	Inkjet printing	2×10^{-5}	0.1 V	NA	1450	<17,200	[70]
	CsPbI$_2$Br	Polycrystals	ALS process	0.04	125	1.14	148,000	280	[74]
	Cs$_{0.1}$(FA$_{0.83}$MA$_{0.17}$)$_{0.9}$Pb(Br$_{0.17}$I$_{0.83}$)$_3$	Polycrystals	Inkjet printing	3.7×10^{-3}	27	2.0×10^{-6}	59.9	12,000	[69]
	Cs$_2$TeI$_6$	Polycrystals	Electro-spraying	1.5×10^{-3}	6670	NA	227	115	[73]
	Cs$_2$ABiBr$_6$/(C$_{38}$H$_{34}$P$_2$)MnBr$_4$	Polycrystals	Tablet pressing	1.7	100	8.5×10^{-5}	114	200	[71]

ITC: inverse temperature crystallization, LTC: low-temperature crystallization, SSCE: secondary solution constant temperature evaporation, ALS: aerosol–liquid–solid.

References

1. Hoheisel, M. Review of medical imaging with emphasis on X-ray detectors. *Nucl. Instrum. Methods Phys. Res. Sect. A Accel. Spectrom. Detect. Assoc. Equip.* **2006**, *563*, 215–224. [CrossRef]
2. Zhou, Y.; Chen, J.; Bakr, O.M.; Mohammed, O.F. Metal Halide Perovskites for X-ray Imaging Scintillators and Detectors. *ACS Energy Lett.* **2021**, *6*, 739–768. [CrossRef]
3. Nikl, M.; Yoshikawa, A. Recent R&D Trends in Inorganic Single-Crystal Scintillator Materials for Radiation Detection. *Adv. Opt. Mater.* **2015**, *3*, 463–481.
4. Weber, M.J. Inorganic scintillators: Today and tomorrow. *J. Lumin.* **2002**, *100*, 35–45. [CrossRef]
5. Maddalena, F.; Xie, A.; Arramel; Witkowski, M.E.; Makowski, M.; Mahler, B.; Drozdowski, W.; Mariyappan, T.; Springham, S.V.; Coquet, P.; et al. Effect of commensurate lithium doping on the scintillation of two-dimensional perovskite crystals. *J. Mater. Chem. C* **2021**, *9*, 2504–2512. [CrossRef]
6. Chen, Q.; Wu, J.; Ou, X.; Huang, B.; Almutlaq, J.; Zhumekenov, A.A.; Guan, X.; Han, S.; Liang, L.; Yi, Z.; et al. All-inorganic perovskite nanocrystal scintillators. *Nature* **2018**, *561*, 88–93. [CrossRef]
7. Almeida, G.; Infante, I.; Manna, L. Resurfacing halide perovskite nanocrystals. *Science* **2019**, *364*, 833–834. [CrossRef]
8. Quan, L.N.; García de Arquer, F.P.; Sabatini, R.P.; Sargent, E.H. Perovskites for light emission. *Adv. Mater.* **2018**, *30*, 1801996. [CrossRef]
9. Voloshinovskii, A.S.; Mikhailik, V.B.; Myagkota, S.V.; Pidzyrailo, M.S.; Pashuk, I.P. Exciton luminescence of ionic semiconductors $CsPbX_3$ (X = Cl, Br, I). *Ukr. J. Phys.* **1993**, *38*, 1012–1015.
10. Belsky, A.; Chevallier, P.; Dhez, P.; Martin, P.; Pédrini, C.; Vasil'Ev, A. X-ray excitation of luminescence of scintillator materials in the 7–22 keV region. *Nucl. Instrum. Methods Phys. Res. Sect. A Accel. Spectrom. Detect. Assoc. Equip.* **1995**, *361*, 384–387. [CrossRef]
11. Shibuya, K.; Koshimizu, M.; Takeoka, Y.; Asai, K. Scintillation properties of $(C_6H_{13}NH_3)_2PbI_4$: Exciton luminescence of an organic/inorganic multiple quantum well structure compound induced by 2.0 MeV protons. *Nucl. Instrum. Methods Phys. Res. Sect. B Beam Interact. Mater. At.* **2002**, *194*, 207–212. [CrossRef]
12. Huang, H.; Abbaszadeh, S. Recent Developments of Amorphous Selenium-Based X-ray Detectors: A Review. *IEEE Sens. J.* **2019**, *20*, 1694–1704. [CrossRef]
13. Schieber, M.; Zuck, A.; Gilboa, H.; Zentai, G. Reviewing Polycrystalline Mercuric Iodide X-ray Detectors. *IEEE Trans. Nucl. Sci.* **2006**, *53*, 2385–2391. [CrossRef]
14. Yun, M.-S.; Cho, S.-H.; Lee, R.; Jang, G.-W.; Kim, Y.-S.; Shin, W.-J.; Nam, S.-H. Investigation of PbI2 Film Fabricated by a New Sedimentation Method as an X-ray Conversion Material. *Jpn. J. Appl. Phys.* **2010**, *49*, 041801. [CrossRef]
15. Kabir, M. Effects of charge carrier trapping on polycrystalline PbO X-ray imaging detectors. *J. Appl. Phys.* **2008**, *104*, 074506. [CrossRef]
16. Szeles, C. CdZnTe and CdTe materials for X-ray and gamma ray radiation detector applications. *Phys. Status Solidi B* **2004**, *241*, 783–790. [CrossRef]
17. Wei, H.; Huang, J. Halide lead perovskites for ionizing radiation detection. *Nat. Commun.* **2019**, *10*, 1–12. [CrossRef]
18. Xu, X.; Qian, W.; Xiao, S.; Wang, J.; Zheng, S.; Yang, S. Halide perovskites: A dark horse for direct X-ray imaging. *EcoMat* **2020**, *2*, e12064. [CrossRef]
19. Zhang, H.; Ji, X.; Yao, H.; Fan, Q.; Yu, B.; Li, J. Review on efficiency improvement effort of perovskite solar cell. *Sol. Energy* **2022**, *233*, 421–434. [CrossRef]
20. SSchmidt-Mende, L.; Dyakonov, V.; Olthof, S.; Ünlü, F.; Lê, K.M.T.; Mathur, S.; Karabanov, A.D.; Lupascu, D.C.; Herz, L.M.; Hinderhofer, A.; et al. Roadmap on organic–inorganic hybrid perovskite semiconductors and devices. *APL Mater.* **2021**, *9*, 109202. [CrossRef]
21. Stoumpos, C.C.; Malliakas, C.D.; Peters, J.A.; Liu, Z.; Sebastian, M.; Im, J.; Chasapis, T.C.; Wibowo, A.C.; Chung, D.Y.; Freeman, A.J.; et al. Crystal Growth of the Perovskite Semiconductor $CsPbBr_3$: A New Material for High-Energy Radiation Detection. *Cryst. Growth Des.* **2013**, *13*, 2722–2727. [CrossRef]
22. Kim, Y.C.; Kim, K.H.; Son, D.-Y.; Jeong, D.-N.; Seo, J.-Y.; Choi, Y.S.; Han, I.T.; Lee, S.Y.; Park, N.-G. Printable organometallic perovskite enables large-area, low-dose X-ray imaging. *Nature* **2017**, *550*, 87–91. [CrossRef]

23. Pan, W.; Yang, B.; Niu, G.; Xue, K.H.; Du, X.; Yin, L.; Zhang, M.; Wu, H.; Miao, X.S.; Tang, J. Hot-Pressed $CsPbBr_3$ Quasi-Monocrystalline Film for Sensitive Direct X-ray Detection. *Adv. Mater.* **2019**, *31*, 1904405. [CrossRef]

24. Glushkova, A.; Andričević, P.; Smajda, R.; Náfrádi, B.; Kollár, M.; Djokić, V.; Arakcheeva, A.; Forró, L.; Pugin, R.; Horváth, E. Ultrasensitive 3D Aerosol-Jet-Printed Perovskite X-ray Photodetector. *ACS Nano* **2021**, *15*, 4077–4084. [CrossRef]

25. Shockley, W. Problems related top-n junctions in silicon. *Czechoslov. J. Phys.* **1961**, *11*, 81–121. [CrossRef]

26. Kakavelakis, G.; Gedda, M.; Panagiotopoulos, A.; Kymakis, E.; Anthopoulos, T.D.; Petridis, K. Metal Halide Perovskites for High-Energy Radiation Detection. *Adv. Sci.* **2020**, *7*, 2002098. [CrossRef]

27. Uxa, Š.; Grill, R.; Belas, E. Evaluation of the mobility-lifetime product in CdTe and CdZnTe detectors by the transient-current technique. *J. Appl. Phys.* **2013**, *114*, 094511. [CrossRef]

28. Basiricò, L.; Ciavatti, A.; Fraboni, B. Solution-Grown Organic and Perovskite X-ray Detectors: A New Paradigm for the Direct Detection of Ionizing Radiation. *Adv. Mater. Technol.* **2020**, *6*, 2000475. [CrossRef]

29. Yang, T.; Li, F.; Zheng, R. Recent advances in radiation detection technologies enabled by metal-halide perovskites. *Mater. Adv.* **2021**, *2*, 6744–6767. [CrossRef]

30. Thompson, M.; Ellison, S.L.R.; Wood, R. Harmonized guidelines for single-laboratory validation of methods of analysis (IUPAC Technical Report). *Pure Appl. Chem.* **2002**, *74*, 835–855. [CrossRef]

31. Song, Y.; Li, L.; Bi, W.; Hao, M.; Kang, Y.; Wang, A.; Wang, Z.; Li, H.; Li, X.; Fang, Y.; et al. Atomistic surface passivation of $CH_3NH_3PbI_3$ perovskite single crystals for highly sensitive coplanar-structure x-ray detectors. *Research* **2020**, *2020*, 5958243. [CrossRef]

32. Wang, W.; Meng, H.; Qi, H.; Xu, H.; Du, W.; Yang, Y.; Yi, Y.; Jing, S.; Xu, S.; Hong, F. Electronic-Grade High-Quality Perovskite Single Crystals by a Steady Self-Supply Solution Growth for High-Performance X-ray Detectors. *Adv. Mater.* **2020**, *32*, 2001540. [CrossRef] [PubMed]

33. Huang, Y.; Qiao, L.; Jiang, Y.; He, T.; Long, R.; Yang, F.; Wang, L.; Lei, X.; Yuan, M.; Chen, J. A-site cation engineering for highly efficient $MAPbI_3$ single-crystal x-ray detector. *Angew. Chem. Int. Ed.* **2019**, *58*, 17834–17842. [CrossRef] [PubMed]

34. Ye, F.; Lin, H.; Wu, H.; Zhu, L.; Huang, Z.; Ouyang, D.; Niu, G.; Choy, W.C. High-quality cuboid CH3NH3PbI3 single crystals for high performance X-ray and photon detectors. *Adv. Funct. Mater.* **2019**, *29*, 1806984. [CrossRef]

35. Geng, X.; Zhang, H.; Ren, J.; He, P.; Zhang, P.; Feng, Q.; Pan, K.; Dun, G.; Wang, F.; Zheng, X.; et al. High-performance single crystal $CH_3NH_3PbI_3$ perovskite x-ray detector. *Appl. Phys. Lett.* **2021**, *118*, 063506. [CrossRef]

36. Shrestha, S.; Fischer, R.; Matt, G.J.; Feldner, P.; Michel, T.; Osvet, A.; Levchuk, I.; Merle, B.; Golkar, S.; Chen, H.; et al. High-performance direct conversion X-ray detectors based on sintered hybrid lead triiodide perovskite wafers. *Nat. Photonics* **2017**, *11*, 436–440. [CrossRef]

37. Geng, X.; Feng, Q.; Zhao, R.; Hirtz, T.; Dun, G.; Yan, Z.; Ren, J.; Zhang, H.; Liang, R.; Tian, H.; et al. High-Quality Single Crystal Perovskite for Highly Sensitive X-ray Detector. *IEEE Electron. Device Lett.* **2019**, *41*, 256–259. [CrossRef]

38. Xu, Q.; Shao, W.; Li, Y.; Zhang, X.; Ouyang, X.; Liu, J.; Liu, B.; Wu, Z.-Y.; Ouyang, X.; Tang, X.; et al. High-Performance Surface Barrier X-ray Detector Based on Methylammonium Lead Tribromide Single Crystals. *ACS Appl. Mater. Interfaces* **2019**, *11*, 9679–9684. [CrossRef]

39. Pan, Y.; Wang, X.; Zhao, J.; Xu, Y.; Li, Y.; Li, Q.; Zhang, X.; Zhao, Z.; Zhu, Z.; Jing, C. Photodiodes based on a $MAPbBr^3$/Bi^{3+}-doped $MAPbCl_3$ single crystals heterojunction for the X-ray detection. *CrystEngComm* **2021**, *23*, 4954–4962. [CrossRef]

40. Fan, Z.; Liu, J.; Zuo, W.; Liu, G.; He, X.; Luo, K.; Ye, Q.; Liao, C. Mixed-Cation $MA_xCs_{1-x}PbBr_3$ Perovskite Single Crystals with Composition Management for High-Sensitivity X-ray Detection. *Phys. Status Solidi (RRL)–Rapid Res. Lett.* **2020**, *14*, 2000226. [CrossRef]

41. Liu, Y.; Zhang, Y.; Zhu, X.; Feng, J.; Spanopoulos, I.; Ke, W.; He, Y.; Ren, X.; Yang, Z.; Xiao, F. Triple-Cation and Mixed-Halide Perovskite Single Crystal for High-Performance X-ray Imaging. *Adv. Mater.* **2021**, *33*, 2006010. [CrossRef]

42. Basiricò, L.; Senanayak, S.P.; Ciavatti, A.; Abdi-Jalebi, M.; Fraboni, B.; Sirringhaus, H. Detection of X-rays by solution-processed cesium-containing mixed triple cation perovskite thin films. *Adv. Funct. Mater.* **2019**, *29*, 1902346. [CrossRef]

43. Possanzini, L.; Basiricò, L.; Ciavatti, A.; Tessarolo, M.; Fraboni, B. Fully Textile X-ray Detectors Based on Fabric-Embedded Perovskite Crystals. *Adv. Mater. Interfaces* **2022**, *9*, 2101417. [CrossRef]

44. Fan, Z.; Liu, J.; Zuo, W.; Liu, G.; He, X.; Luo, K.; Ye, Q.; Liao, C. Solution-Processed $MAPbBr_3$ and $CsPbBr_3$ Single-Crystal Detectors with Improved X-ray Sensitivity via Interfacial Engineering. *Phys. Status Solidi A* **2020**, *217*, 2000104. [CrossRef]

45. Zhang, H.; Wang, F.; Lu, Y.; Sun, Q.; Xu, Y.; Zhang, B.-B.; Jie, W.; Kanatzidis, M.G. High-sensitivity X-ray detectors based on solution-grown caesium lead bromide single crystals. *J. Mater. Chem. C* **2020**, *8*, 1248–1256. [CrossRef]

46. Peng, J.; Xia, C.Q.; Xu, Y.; Li, R.; Cui, L.; Clegg, J.K.; Herz, L.M.; Johnston, M.B.; Lin, Q. Crystallization of $CsPbBr_3$ single crystals in water for X-ray detection. *Nat. Commun.* **2021**, *12*, 1531. [CrossRef] [PubMed]

47. Heo, J.H.; Shin, D.H.; Park, J.K.; Kim, D.H.; Lee, S.J.; Im, S.H. High-Performance Next-Generation Perovskite Nanocrystal Scintillator for Nondestructive X-ray Imaging. *Adv. Mater.* **2018**, *30*, e1801743. [CrossRef] [PubMed]

48. Gou, Z.; Huanglong, S.; Ke, W.; Sun, H.; Tian, H.; Gao, X.; Zhu, X.; Yang, D.; Wangyang, P. Self-Powered X-ray Detector Based on All-Inorganic Perovskite Thick Film with High Sensitivity under Low Dose Rate. *Phys. Status Solidi (RRL)–Rapid Res. Lett.* **2019**, *13*, 1900094. [CrossRef]

49. Matt, G.J.; Levchuk, I.; Knüttel, J.; Dallmann, J.; Osvet, A.; Sytnyk, M.; Tang, X.; Elia, J.; Hock, R.; Heiss, W.; et al. Sensitive Direct Converting X-ray Detectors Utilizing Crystalline $CsPbBr_3$ Perovskite Films Fabricated via Scalable Melt Processing. *Adv. Mater. Interfaces* **2020**, *7*, 1901575. [CrossRef]

50. Lai, P.-T.; Lin, H.-C.; Chuang, Y.-T.; Chen, C.-Y.; Cheng, W.-K.; Tan, G.-H.; Hsu, B.-W.; Yang, L.; Lou, S.-C.; Chien, L.-J.; et al. All-Vacuum-Deposited Perovskite X-ray Detector with a Record-High Self-Powered Sensitivity of 1.2 C Gy^{-1} cm^{-3}. *ACS Appl. Mater. Interfaces* **2022**, *14*, 19795–19805. [CrossRef] [PubMed]

51. Lédée, F.; Ciavatti, A.; Verdi, M.; Basiricò, L.; Fraboni, B. Ultra-Stable and Robust Response to X-rays in 2D Layered Perovskite Micro-Crystalline Films Directly Deposited on Flexible Substrate. *Adv. Opt. Mater.* **2022**, *10*, 2101145. [CrossRef]

52. Shi, E.; Gao, Y.; Finkenauer, B.P.; Akriti, A.; Coffey, A.H.; Dou, L. Two-dimensional halide perovskite nanomaterials and heterostructures. *Chem. Soc. Rev.* **2018**, *47*, 6046–6072. [CrossRef]

53. Li, H.; Song, J.; Pan, W.; Xu, D.; Zhu, W.; Wei, H.; Yang, B. Sensitive and STable 2D Perovskite Single-Crystal X-ray Detectors Enabled by a Supramolecular Anchor. *Adv. Mater.* **2020**, *32*, 2003790. [CrossRef] [PubMed]

54. Qian, C.X.; Wang, M.Z.; Lu, S.S.; Feng, H.J. Fabrication of 2D perovskite (PMA) 2PbI$_4$ crystal and Cu ion implantation improved X-ray detector. *Appl. Phys. Lett.* **2022**, *120*, 011901. [CrossRef]

55. Li, M.; Li, H.; Li, W.; Li, B.; Lu, T.; Feng, X.; Guo, C.; Zhang, H.; Wei, H.; Yang, B. Oriented 2D Perovskite Wafers for Anisotropic X-ray Detection through a Fast Tableting Strategy. *Adv. Mater.* **2022**, *34*, 2108020. [CrossRef] [PubMed]

56. Ji, C.; Wang, S.; Wang, Y.; Chen, H.; Li, L.; Sun, Z.; Sui, Y.; Wang, S.; Luo, J. 2D Hybrid Perovskite Ferroelectric Enables Highly Sensitive X-ray Detection with Low Driving Voltage. *Adv. Funct. Mater.* **2019**, *30*, 1905529. [CrossRef]

57. Tsai, H.; Liu, F.; Shrestha, S.; Fernando, K.; Tretiak, S.; Scott, B.; Vo, D.T.; Strzalka, J.; Nie, W. A sensitive and robust thin-film X-ray detector using 2D layered perovskite diodes. *Sci. Adv.* **2020**, *6*, eaay0815. [CrossRef]

58. Tsai, H.; Shrestha, S.; Pan, L.; Huang, H.-H.; Strzalka, J.; Williams, D.; Wang, L.; Cao, L.R.; Nie, W. Quasi-2D Perovskite Crystalline Layers for Printable Direct Conversion X-ray Imaging. *Adv. Mater.* **2022**, *34*, 2106498. [CrossRef]

59. Zhang, B.-B.; Liu, X.; Xiao, B.; Ben Hafsia, A.; Gao, K.; Xu, Y.; Zhou, J.; Chen, Y. High-Performance X-ray Detection Based on One-Dimensional Inorganic Halide Perovskite CsPbI$_3$. *J. Phys. Chem. Lett.* **2019**, *11*, 432–437. [CrossRef] [PubMed]

60. Xu, Y.; Jiao, B.; Song, T.B.; Stoumpos, C.C.; He, Y.; Hadar, I.; Lin, W.; Kanatzidis, M.G. Zero-dimensional Cs$_2$TeI$_6$ perovskite: Solution-processed thick films with high X-ray sensitivity. *ACS Photonics* **2018**, *6*, 196–203. [CrossRef]

61. Xu, Q.; Li, C.; Nie, J.; Guo, Y.; Wang, X.; Zhang, B.; Ouyang, X. Highly Sensitive and Stable X-ray Detector Based on a 0D Structural Cs$_4$PbI$_6$ Single Crystal. *J. Phys. Chem. Lett.* **2020**, *12*, 287–293. [CrossRef]

62. Steele, J.A.; Pan, W.; Martin, C.; Keshavarz, M.; Debroye, E.; Yuan, H.; Banerjee, S.; Fron, E.; Jonckheere, D.; Kim, C.W.; et al. Photophysical Pathways in Highly Sensitive Cs$_2$AgBiBr$_6$ Double-Perovskite Single-Crystal X-ray Detectors. *Adv. Mater.* **2018**, *30*, 1804450. [CrossRef]

63. Pan, W.; Wu, H.; Luo, J.; Deng, Z.; Ge, C.; Chen, C.; Jiang, X.; Yin, W.-J.; Niu, G.; Zhu, L.; et al. Cs$_2$AgBiBr$_6$ single-crystal X-ray detectors with a low detection limit. *Nat. Photonics* **2017**, *11*, 726–732. [CrossRef]

64. Yuan, W.; Niu, G.; Xian, Y.; Wu, H.; Wang, H.; Yin, H.; Liu, P.; Li, W.; Fan, J. In Situ regulating the order–disorder phase transition in Cs$_2$AgBiBr$_6$ single crystal toward the application in an X-ray detector. *Adv. Funct. Mater.* **2019**, *29*, 1900234. [CrossRef]

65. Zhuang, R.; Wang, X.; Ma, W.; Wu, Y.; Chen, X.; Tang, L.; Zhu, H.; Liu, J.; Wu, L.; Zhou, W.; et al. Highly sensitive X-ray detector made of layered perovskite-like (NH$_4$)$_3$Bi$_2$I$_9$ single crystal with anisotropic response. *Nat. Photonics* **2019**, *13*, 602–608. [CrossRef]

66. Dong, S.; Xin, D.; Zhang, M.; Tie, S.; Cai, B.; Ma, Q.; Zheng, X. Green solvent blade-coated MA$_3$Bi$_2$I$_9$ for direct-conversion X-ray detectors. *J. Mater. Chem. C* **2022**, *10*, 6236–6242. [CrossRef]

67. Li, W.; Xin, D.; Tie, S.; Ren, J.; Dong, S.; Lei, L.; Zheng, X.; Zhao, Y.; Zhang, W. Zero-Dimensional Lead-Free FA$_3$Bi$_2$I$_9$ Single Crystals for High-Performance X-ray Detection. *J. Phys. Chem. Lett.* **2021**, *12*, 1778–1785. [CrossRef]

68. Zhang, Y.; Liu, Y.; Xu, Z.; Ye, H.; Yang, Z.; You, J.; Liu, M.; He, Y.; Kanatzidis, M.G.; Liu, S. Nucleation-controlled growth of superior lead-free perovskite Cs3Bi2I9 single-crystals for high-performance X-ray detection. *Nat. Commun.* **2020**, *11*, 1–11.

69. Mescher, H.; Schackmar, F.; Eggers, H.; Abzieher, T.; Zuber, M.; Hamann, E.; Baumbach, T.; Richards, B.S.; Hernandez-Sosa, G.; Paetzold, U.W.; et al. Flexible Inkjet-Printed Triple Cation Perovskite X-ray Detectors. *ACS Appl. Mater. Interfaces* **2020**, *12*, 15774–15784. [CrossRef]

70. Liu, J.; Shabbir, B.; Wang, C.; Wan, T.; Ou, Q.; Yu, P.; Tadich, A.; Jiao, X.; Chu, D.; Qi, D.; et al. Flexible, printable soft-X-ray detectors based on all-inorganic perovskite quantum dots. *Adv. Mater.* **2019**, *31*, 1901644. [CrossRef] [PubMed]

71. Li, W.; Liu, L.; Tan, M.; He, Y.; Guo, C.; Zhang, H.; Wei, H.; Yang, B. Low-Cost and Large-Area Hybrid X-ray Detectors Combining Direct Perovskite Semiconductor and Indirect Scintillator. *Adv. Funct. Mater.* **2021**, *31*, 2107843. [CrossRef]

72. Ciavatti, A.; Sorrentino, R.; Basiricò, L.; Passarella, B.; Caironi, M.; Petrozza, A.; Fraboni, B. High-Sensitivity Flexible X-ray Detectors based on Printed Perovskite Inks. *Adv. Funct. Mater.* **2021**, *31*, 2009072. [CrossRef]

73. Guo, J.; Chen, S.; Xu, Y.; Li, F.; Jie, W.; Zhu, M. Oriented preparation of Large-Area uniform Cs$_2$TeI$_6$ perovskite film for high performance X-ray detector. *J. Colloid Interface Sci.* **2022**, *624*, 629–636. [CrossRef] [PubMed]

74. Qian, W.; Xu, X.; Wang, J.; Xu, Y.; Chen, J.; Ge, Y.; Chen, J.; Xiao, S.; Yang, S. An aerosol-liquid-solid process for the general synthesis of halide perovskite thick films for direct-conversion X-ray detectors. *Matter* **2021**, *4*, 942–954. [CrossRef]